

# Multi-output calibration of a honeycomb seal via on-site surrogates

Jiangeng Huang\*

Robert B. Gramacy†

## Abstract

We consider large-scale industrial computer model calibration, combining multi-output simulation with limited physical observation, involved in the development of a honeycomb seal. Toward that end, we adopt a localized sampling and emulation strategy called “on-site surrogates (OSSs)”, designed to cope with the amalgamated challenges of high-dimensional inputs, large-scale simulation campaigns, and nonstationary response surfaces. In previous applications, OSSs were one-at-a-time affairs for multiple outputs. We demonstrate that this leads to dissonance in calibration efforts for a common parameter set across outputs for the honeycomb. Instead, a conceptually straightforward, but implementationally intricate, principal-components representation, adapted from ordinary Gaussian process surrogate modeling to the OSS setting, can resolve this tension. With a two-pronged – optimization-based and fully Bayesian – approach, we show how pooled information across outputs can reduce uncertainty and enhance (statistical and computational) efficiency in calibrated parameters for the honeycomb relative to the previous, “data-poor” univariate analog.

**Keywords:** Bayesian calibration, multivariate analysis, computer experiment, hierarchical model, big data, surrogate modeling, uncertainty quantification

## 1 Introduction

Computer simulation experiments play an increasingly pivotal role in scientific inquiry. STEM training, cheap hardware, and robust numerical libraries have democratized simulation as a means of exploration of complex physical (e.g., Mehta et al., 2014), biological (e.g., Johnson, 2008), engineering/materials (e.g., Zhang et al., 2015), and economic phenomena (e.g., Kita et al., 2016), to provide a few representative examples. Simulation in industry borrows elements from all of the above depending on the nature of application/business.

---

\*Genentech, Inc., South San Francisco, CA 94080

†Department of Statistics, Virginia Tech

We are interested in the use of simulation in the development of a so-called *honeycomb seal*, a device integral to oil and gas recovery, together with colleagues at Baker Hughes, a General Electric company (BHGE). The honeycomb experiment mirrors a common setup in engineering applications, leveraging a general purpose simulator called **ISOTSEAL**, a commercial spin-off of tools developed first at Texas A&M (Kleynhans and Childs, 1997).

Adapting a general-purpose solver like **ISOTSEAL** to a particular application like BHGE’s honeycomb is often a two-stage process. One first adapts configuration files to reflect the known design and operational parameters/conditions of the particular instance under study. Inevitably some of these computer model settings are unknown (precisely enough) in the actual system, so there is interest in *calibrating* these parameters based a limited physical/field experimentation campaign. Simulations, collected under a range of settings of both unknown *calibration parameters* and known *design inputs* characterizing operating conditions, can then be “matched” with analogs observed in the field, and their residuals can drive inference for the unknown settings, comprising the second stage.

Although there are several ways to operationalize that idea, the canonical setup in the computer experiments literature is due to Kennedy and O’Hagan (2001, KOH hereafter). At a high level, with details in Section 2, KOH couples two Gaussian processes (GPs) together – one as a surrogate for the computer model (e.g., **ISOTSEAL**), and another to capture bias and noise between simulation and field observation, to form a multivariate normal (MVN) marginal likelihood which can drive inference for all unknowns, including the calibration parameters. KOH offers a nice synthesis of information sources, but is susceptible to confounding (e.g., Brynjarsdóttir and O’Hagan, 2014; Tuo and Wu, 2016; Plumlee, 2017; Gu, 2019). More important for us, however, is that it is computationally daunting. Cubic matrix decompositions for MVNs involved in GP-based inference will severely limit the size of simulation campaigns that can be entertained in this setting (See Santner et al. (2018); Gramacy (2020)). Historically, computer simulation was cumbersome, limiting the size of campaigns. Nowadays that’s changing.

The **ISOTSEAL** simulator is fast, so a big campaign is reasonable computationally, but not so fast nor steady enough that simulations can be used directly (forgoing the surrogate) in an otherwise KOH-style setting (Higdon et al., 2004). Meanwhile a large simulation campaign is essential to capture stark changes in dynamics, simulation artifacts, and other “features” common to modern numerical solvers. A flexible meta-modeling apparatus is essential in order to cope with large training data sizes, and to adapt to and/or smooth over (i.e., separate signal from) “noise”/artifacts in such settings. Huang et al. (2020) proposed one such approach based on *on-site surrogates* (OSSs), motivated specifically by **ISOTSEAL** and the BHGE honeycomb, but also vetted generically in benchmark exercises. Huang et al. showed how the KOH apparatus, and variations based on modularization (Liu et al., 2009) and maximization (Gramacy et al., 2015), could be adapted to work with OSSs.

Although promising, this setup was only designed to calibrate for one output feature at a time and honeycomb/**ISOTSEAL** output is multi-dimensional. Our BHGE collaborators are interested in at least four frequencies of outputs on four properties of the system (16 total). Section 3 demonstrates the inadequacy of a one-at-a-time approach to calibrating outputs independently, leading to inconsistent inference about calibration parameters, thus challenging downstream data synthesis, which stems from honeycomb’s unique architecture and (simulated and real) dynamics. This happens because the physical dynamics in play are complex, and the imposition of complete independence across property and frequency throws too much information away.

KOH has subsequently been extended to multi-output simulation and field experimentation (e.g. Higdon et al., 2008), but with ordinary GP surrogates. In this paper we detail the application of OSSs in that context, which is easier said than done. Although the basic ingredients are similar to Higdon et al., via principal component decompositions, their application is non-trivial in this setting and requires care in methodological development as well as implementation, as we provide. Following Huang et al. (2020), we take a two-pronged approach: first via thrifty marginalize–maximize calculations, rather than faithful

KOH, then full Bayes with MCMC. The result is a multi-output, large-scale, computer model calibration framework that – at least in the case of the honeycomb – is demonstrably able to resolve stark multi-output calibration inconsistencies by making effective use of the (joint) information in all of the available simulation and field data.

The remainder of paper is organized as follows. Section 2 begins with review of basics, like KOH and GPs, and multi-output (ordinary GP) calibration. Honeycomb specifics and univariate OSS calibration review is in Section 3, establishing the straw man. Section 4 combines these building blocks for calibration with multivariate outputs via OSSs leveraging linear dependence across output frequency. Thrifty modular and fully Bayesian KOH are enumerated in turn. Section 5 combines across output property and provides honeycomb’s multi-output calibration results. Section 6 concludes with a discussion.

## 2 Review of elements

We introduce KOH calibration via GPs, and extensions for scale and multivariate output.

### 2.1 Basics: calibration and surrogate modeling

Kennedy and O’Hagan (2001) described a univariate Bayesian calibration framework, combining field experimental observations  $y^F(\mathbf{x})$ , at a vector of input design variables  $\mathbf{x}$ , with computer simulations  $y^M(\mathbf{x}, \mathbf{u}^*)$ , under ideal or “true” calibration/tuning parameter(s)  $\mathbf{u}^*$ , through a discrepancy or bias correction  $b(\mathbf{x})$ , between simulation and field observation:

$$y^F(\mathbf{x}) = y^M(\mathbf{x}, \mathbf{u}^*) + b(\mathbf{x}) + \epsilon, \quad \epsilon \stackrel{\text{iid}}{\sim} \mathcal{N}(0, \sigma_\epsilon^2). \quad (1)$$

Modeling and inference commences via Gaussian processes (GP) priors on  $y^M(\mathbf{x}, \mathbf{u}^*)$  and  $b(\mathbf{x})$ . GPs provide a flexible nonparametric (Bayesian) structure for smooth functional relationships between inputs  $\mathbf{x}$  and output  $f(\mathbf{x})$ , where any finite number  $N$  of evaluations

follow a multivariate normal (MVN) distribution:  $f(\mathbf{x}) \sim \mathcal{N}_N(\mu(\mathbf{x}), \Sigma(\mathbf{x}, \mathbf{x}'))$ . Inference for any aspect of  $\mu$  and  $\Sigma$  given training data  $\mathbf{D}_N = (\mathbf{X}_N, \mathbf{y}_N)$  may be facilitated by likelihoods, i.e., MVN densities. Often in practice  $\mu(\cdot) = 0$ . MVN density/likelihood evaluation for aspects of  $\Sigma$ , which is usually based on inverse Euclidean distance up to several unknown hyperparameters  $\phi$  involve cubic-in- $N$  matrix decomposition for inverses and determinants, which can be a bottleneck in large-scale applications.

This is exacerbated in the KOH setting where Eq. (1) implies a joint distribution for computer model training data  $\mathbf{D}_{NM} = (\mathbf{X}_{NM}, \mathbf{y}_{NM})$  and field data  $\mathbf{D}_{NF} = (\mathbf{X}_{NF}, \mathbf{y}_{NF})$ :

$$\begin{bmatrix} \mathbf{y}_{NM} \\ \mathbf{y}_{NF} \end{bmatrix} \sim \mathcal{N}_{N_M+N_F}(\mathbf{0}, \Sigma(\mathbf{u})), \quad \text{where} \quad \Sigma(\mathbf{u}) \equiv \begin{bmatrix} \Sigma_{NM} & \Sigma_{NF, NM}^\top(\mathbf{u}) \\ \Sigma_{NF, NM}(\mathbf{u}) & \Sigma_{NF}(\mathbf{u}) + \Sigma_{NF}^b \end{bmatrix}. \quad (2)$$

In (2) above,  $\Sigma_{NM} \equiv \Sigma([\mathbf{X}_{NM}, \mathbf{U}_{NM}])$  is an  $N_M \times N_M$  covariance matrix for simulations  $y^M(\cdot)$ , capturing pairwise covariance between  $p_x + p_u$  dimensional inputs  $(\mathbf{x}, \mathbf{u})$ , and  $\mathbf{U}_{NM} \equiv [\mathbf{u}_1^\top, \dots, \mathbf{u}_{N_M}^\top]$  stacks  $N_M$  length  $p_u$  row vectors. The off-diagonal  $\Sigma_{NF, NM}(\mathbf{u})$  is an  $N_F \times N_M$  matrix capturing covariance between simulation inputs  $[\mathbf{X}_{NM}, \mathbf{U}_{NM}]$  and field inputs  $[\mathbf{X}_{NF}, \mathbf{U}_{NF}]$ , again under  $y^M(\cdot)$ , where  $\mathbf{U}_{NF} \equiv [\mathbf{u}_1^\top, \dots, \mathbf{u}_{N_F}^\top]$  stacks  $N_F$  identical row vectors of (unknown) parameters  $\mathbf{u}$ . Similarly,  $\Sigma_{NF}(\mathbf{u}) \equiv \Sigma([\mathbf{X}_{NF}, \mathbf{U}_{NF}])$  is  $N_F \times N_F$  for  $[\mathbf{X}_{NF}, \mathbf{U}_{NF}]$ ,  $y^M(\cdot)$  dynamics between field data observations. Lastly,  $\Sigma_{NF}^b$  is an  $N_F \times N_F$  matrix of covariances specified by the bias correction GP  $\hat{b}(\mathbf{x})$  acting only on field inputs  $\mathbf{X}_{NF}$ .

Under these coupled GPs, fully Bayesian inference for unknown  $\mathbf{u}$  under prior  $p(\mathbf{u})$ , generically, hinges on  $p(\mathbf{y}_{NM}, \mathbf{y}_{NF} \mid \mathbf{u})$ , the MVN (marginal) likelihood implied by Eq. (2). The main computational challenges are evident in inverse  $\Sigma^{-1}(\mathbf{u})$  and determinant  $|\Sigma(\mathbf{u})|$  evaluations involved in such density evaluations. A single Cholesky decomposition could furnish both in  $\mathcal{O}((N_M + N_F)^3)$  flops. Holding covariance parameters fixed, notice that not all blocks of  $\Sigma(\mathbf{u})$  change as  $\mathbf{u}$  varies. While this implies potential for several economies, the computational demands are still substantial (e.g., cubic in  $N_M \gg N_F$ ) and nonetheless

requires  $\mathcal{O}((N_M + N_F)^2)$  for storage. For more details see Gramacy (2020, Section 8.1).

However, if computational hurdles can be surmounted, synthesis of information at varying fidelity (i.e., over field and simulation) can be a highly lucrative affair in spite of notorious identifiability challenges in the tussle between estimated calibration parameters  $\hat{\mathbf{u}}$  and model discrepancies  $\hat{b}(\mathbf{x})$ , with remedies of varying degree coming in Bayesian (Higdon et al., 2004; Plumlee, 2017; Brynjarsdóttir and O'Hagan, 2014; Gu and Wang, 2018) and frequentist (Tuo and Wu, 2015, 2016; Wong et al., 2017; Plumlee, 2019) flavors. One of the most basic of these, due to Liu et al. (2009), is known as *modularization*. Modularized Bayesian calibration imposes partial independence on the joint MVN KOH structure, separating a surrogate for  $\hat{y}(\mathbf{x}, \mathbf{u})$  and bias  $\hat{b}(\mathbf{x})$  into two distinct phases.

## 2.2 Scaling up

Besides other philosophical advantages, the modular setup allows for thriftier surrogate modeling, and thus more tractable posterior inference for  $\mathbf{u}$  in large-data settings. Gramacy et al. (2015) leveraged modularization into an very large radiative shock hydrodynamics experiment via local approximate Gaussian processes (LAGP Gramacy and Apley, 2015). LAGP uses a neighborhood of  $n_M \ll N_M$  nearby data subsets for much faster inference.

$$\begin{array}{ccc} \hat{\mathbf{y}}_{N_M}^M(\mathbf{X}_{N_M}^M, \mathbf{U}_{N_M}) & \longrightarrow & \hat{\mathbf{y}}_{n_M}^M(\mathbf{X}_{n_M}^M, \mathbf{U}_{n_M}) \\ \text{Global GP} & \longrightarrow & \text{laGP} \end{array} \quad (3)$$

Inference for  $\mathbf{u}$  proceeds via maximization of the posterior for  $b(\cdot)$  through the observed discrepancy  $\mathbf{D}_{N_F}^B(\mathbf{u}) = (\mathbf{X}_{N_F}^F, \mathbf{y}_{N_F}^F - \hat{\mathbf{y}}_{N_F}^M(\mathbf{u}))$ :

$$\hat{\mathbf{u}} = \arg \max_{\mathbf{u}} \left\{ p(\mathbf{u}) \left[ \max_{\phi_b} p_b(\phi_b \mid \mathbf{D}_{N_F}^B(\mathbf{u})) \right] \right\}, \quad (4)$$

where  $p_b$  is the MVN log (marginal) likelihood for the GP prior on  $b(\cdot)$ , and  $\phi_b$  are any hyperparameters involved in the bias covariance structure, e.g., lengthscales.

Huang et al. (2020) developed on-site surrogates (OSSs), essentially pairing a design strategy with local GP surrogate modeling for KOH. Foreshadowing somewhat, as details are coming shortly in Section 3, they were motivated by the unique characteristics of (cheap/fast but erratic and high-dimensional) **ISOTSEAL** for the honeycomb. Compared to conventional simulators (slow but smooth and low-dimensional) the honeycomb demanded a large **ISOTSEAL** campaign of  $N_M = 292,000$  runs to fully map out the response surface. Yet only a small handful  $N_F = 292$  of field-data observations were available.

To resolve this “too big, too small” dilemma, Huang et al. proposed to design/fit **ISOTSEAL** simulations/surrogates “on-site” as follows: focus simulation designs, separately, on each of the physical experimental input sites  $\mathbf{x}_i$ , for  $i = 1, 2, \dots, N_F$ , paired with space-filling designs at calibration inputs  $\mathbf{u}$  of size  $N_M = 1000$ . Extending chart (3) ...

$$\begin{array}{ccccccc} \hat{\mathbf{y}}_{N_M}^M(\mathbf{X}_{N_M}^M, \mathbf{U}_{N_M}) & \longrightarrow & \hat{\mathbf{y}}_{n_M}^M(\mathbf{X}_{n_M}^M, \mathbf{U}_{n_M}) & \longrightarrow & \hat{\mathbf{y}}_{n_i}^M(\mathbf{U}_{n_i}), i = 1, 2, \dots, N_F \\ \text{Global GP} & \longrightarrow & \text{laGP} & \longrightarrow & \text{OSSs} \end{array} \quad (5)$$

where  $n_i$  denotes the number of **ISOTSEAL** runs at the  $i^{\text{th}}$  site. In this way, the heavy  $p_x + p_u = 17\text{d}$  simulation/emulation cargo is decomposed onto a handful ( $N_F$ ) of lighter, individually focused  $p_u = 4\text{d}$  sites. Consequently, OSSs address computational bottlenecks, provide non-stationary flexibility, automatically smooth over artifacts in some cases, and interpolates dynamics in others. Modularized calibration via maximization (4) for  $\hat{\mathbf{u}}$  is straightforward. OSSs also create a highly sparse kernel for  $\Sigma(\mathbf{u})$  in (2), so fully Bayesian KOH inference  $\mathbf{u}$  is tractable even with  $N_M$  in the millions.

### 2.3 Calibration with multivariate outputs

Although ideal for **ISOTSEAL** in many respects, this OSS strategy was for single-outputs. In Section 3.1 we show that separate application on honeycomb’s multiple outputs (varying frequencies and stiffness/damping coefficients) is problematic, motivating our main

methodological contribution [Section 4]. Generally speaking, high dimensional simulation output can manifest in many ways: functional (Bayarri et al., 2007; Higdon et al., 2008), time series (Conti and O’Hagan, 2010; Fadikar et al., 2018), spatial (Bayarri et al., 2009), spatial-temporal (Gu and Berger, 2016), spectral (Guinness, 2019), with derivatives (McFarland et al., 2008). Besides being inherently more complex, multivariate output naturally implies larger data size, aggravating computational challenges. Yet combining highly multivariate, physically meaningful information, offers the potential for improved posterior concentration and identification in calibration (see, e.g. Arendt et al., 2012; Jiang et al., 2016).

Dimension reduction, utilized appropriately, can help. For example, Higdon et al. (2008) extended univariate KOH into highly multivariate settings through principal components,

$$\mathbf{y}^F(\mathbf{x}) = \mathbf{K}^M \mathbf{w}^M(\mathbf{x}, \mathbf{u}^*) + \mathbf{K}^B \mathbf{w}^B(\mathbf{x}) + \epsilon. \quad (6)$$

In this framework, high dimensional field observations  $\mathbf{y}^F(\mathbf{x})$  are modeled through  $\mathbf{w}^M(\mathbf{x}, \mathbf{u}^*)$  via orthogonal basis matrix  $\mathbf{K}^M$ , and discrepancies  $\mathbf{w}^B(\mathbf{x})$  via  $\mathbf{K}^B$ . Crucially, inference remains tractable via MCMC, at least compared to the single-output analog, and so long as training data sizes ( $N_F, N_M$ ) are moderate. We aim to port this into the OSS framework [Section 4]. Other multi-output calibration approaches, which seem less well-matched to our honeycomb setting, include wavelet bases for functional outputs (Bayarri et al., 2007), and the linear model of co-regionalization (LMC; Paulo et al., 2012).

### 3 Honeycomb specifics

Centrifugal compressors employ seals to minimize leakage in gas compression phases, preventing back flow and consequently performance decay. Conventional annular gas seals, such as labyrinth and abradable seals, cause gas recirculation around the shaft and pro-

duce destabilizing vibration effects. Honeycomb seals are used in high performance turbomachinery to promote stability via damping (see, e.g. Childs, 1993). Here we consider a honeycomb rotor stabilizing gas seal under development at BHGE.

The system under study is characterized by input–output relationships between variables representing seal geometry and flow dynamics. These include  $p_x = 13$  controllable physical design inputs  $\mathbf{x}$ , including rotational speed, cell depth, seal diameter and length, inlet swirl, gas viscosity, gas temperature, compressibility factor, specific heat, inlet/outlet pressure, and inlet/outlet clearance. The field experiment, from BHGE’s component-level honeycomb seal test campaign, comprises  $N_F = 292$  runs varying a subset of those conditions,  $\mathbf{X}_{N_F}$ , believed to have greatest variability during turbomachinery operation: clearance, swirl, cell depth, seal length, and seal diameter. Measured output features include direct/cross stiffness and damping properties at multiple frequencies.

A general-purpose rotordynamic simulator called **ISOTSEAL**, built upon bulk-flow theory, virtually stress seals like the honeycomb. First developed at Texas A&M University (Kleynhans and Childs, 1997), it offers – among other things – fast evaluation (usually about one second) of gas seal force coefficients. Our BHGE colleagues developed an **R** interface mapping the seventeen scalar inputs for the honeycomb seal experiment into the format required for **ISOTSEAL**. Thirteen of those inputs match up with the columns of  $\mathbf{X}_{N_F}$  (i.e., they are  $\mathbf{x}$ ’s); four are calibration parameters  $\mathbf{u}$ , which could not be controlled nor observed in the field. These comprise statoric and rotoric friction coefficients  $n_s, n_r$  and exponents  $m_s, m_r$ . Following Huang et al. (2020), we work with friction factors coded to the unit cube:  $(n_s, m_s, n_r, m_r)^\top \rightarrow (u_1, u_2, u_3, u_4)^\top \in [0, 1]^4$ . This is mostly for practical reasons, but also protects BHGE’s intellectual property.

### 3.1 Multivariate outputs

The potential set of output features that could be monitored for the honeycomb seal are many. Here we focus on four rotordynamic coefficients, or properties: direct stiffness ( $K_d$ ),

cross stiffness ( $k_c$ ), direct damping ( $C_d$ ), and cross damping ( $c_c$ ), measured at the following frequencies: 28, 70, 126, and 154 Hz; so 16 outputs in total. These are our  $\mathbf{y}$ -values, measured either in the field as  $\mathbf{y}_i^F$ , collected as  $\mathbf{Y}_{N_F}$ , or as  $\mathbf{y}_i^M$  simulated via **ISOTSEAL**, collected as  $\mathbf{Y}_{N_M}$ . Huang et al. (2020) only considered one of these:  $K_d$  at 28 Hz.

The turbomachinery literature and bulk-flow theory (Hirs, 1973) provides some insight into the relationship between these four properties. For example, D’Souza and Childs (2002) demonstrate that classical transfer for a honeycomb gas seal process can be expressed in a conventional linear motion/reaction-force model

$$-\begin{bmatrix} F_x \\ F_y \end{bmatrix} = \begin{bmatrix} K_d & k_c \\ -k_c & K_d \end{bmatrix} \begin{bmatrix} x \\ y \end{bmatrix} + \begin{bmatrix} C_d & c_c \\ -c_c & C_d \end{bmatrix} \begin{bmatrix} \dot{x} \\ \dot{y} \end{bmatrix} \quad (\text{units omitted}). \quad (7)$$

Direct stiffness  $K_d$  and damping  $C_d$  account for orthogonal reaction forces in  $x$  and  $y$  axes. Cross-coupled stiffness  $k_c$  and damping  $c_c$  describe reaction orthogonal to directions of motion. Other mechanical engineering studies of rotordynamic coefficients include Childs (1993); Kleynhans and Childs (1997); Delgado et al. (2012).

To access simulated versions of these outputs we augmented BHGE’s R interface for **ISOTSEAL** and then re-ran campaign of Huang et al. (2020), collecting following:

$$\hat{\mathbf{Y}}^M(\mathbf{x}, \mathbf{u}) \equiv \hat{y}_{ijk}^M(\mathbf{u}), \quad \text{for } \begin{cases} i = 1, 2, \dots, N_F \text{ (i.e., each field data pair)} \\ j \in \{1, 2, 3, 4\} \text{ coding properties } \{K_d, k_c, C_d, c_c\} \\ k \in \{1, 2, 3, 4\} \text{ coding frequencies.} \end{cases} \quad (8)$$

In total this involved  $292 \times 1000 \times 4 \approx 1,168,000$  **ISOTSEAL** runs. Each run at inputs  $(\mathbf{x}, \mathbf{u})$  is for a single output frequency, producing all four rotordynamic coefficients simultaneously. In about 2% of cases a convergence issue is detected, terminating with an **NA**-coded missing value after about three seconds. Collecting all 4,672,000 measurements, over the four frequencies, took about three days when divvied up across several multi-core compute

notes. Our experiment resulted in  $N_M = \sum_{i=1}^{N_F} n_i = 286,282$  successfully terminated runs, with most sites (241 out of 292) having a full  $n_i = 1,000$ . Of the 51 with missing responses of varying multitudes, the smallest was  $n_{238} = 574$ . In total, we collected  $16 \times 286,282 = 4,580,512$  on-site multivariate **ISOTSEAL** runs. The missingness pattern is similar to that reported in Huang et al. (2020), even across output coefficients and frequencies because a failed run at a particular input affects all outputs equally. One of the aims of OSS calibration is to extrapolate to these unknown/missing parameter regions after calibrating to field data. See, e.g., Marcy and Storlie (2020), albeit on a somewhat smaller scale.

A 16-fold increase in data, exhibiting all of the features of the single-output case (non-stationarity, missingness, etc.), demands a scale-up of OSS calibration in several directions. We describe that in Section 4, but it shares pre-processing with a separate analysis of each output. We therefore turn first to a description of that simpler process, which ultimately serves as a straw man against our fully multivariate analysis.

### 3.2 Separate univariate analysis

Consider OSSs built separately for each of the outputs. Each OSS comprises a fitted GP between successful on-site **ISOTSEAL** run outputs  $y_{ijk}^M$  at  $\mathbf{x}_i$  and with novel 1,000-element maximin Latin hypercube sample (LHS; Morris and Mitchell, 1995)  $\mathbf{U}_{ijk}$ , for fixed  $j$  and  $k$ . Specifically,  $\hat{y}_{ijk}^M$  is built by fitting a stationary zero-mean GP using a scaled and nugget-augmented separable Gaussian power exponential kernel

$$V_{ijk}(\mathbf{u}_{jk}, \mathbf{u}'_{jk}) = \tau_{ijk}^2 \exp \left\{ - \sum_{l=1}^{p_u} \frac{\|\mathbf{u}_{ijkl} - \mathbf{u}'_{ijkl}\|^2}{\theta_{ijkl}} + \delta_{u,u'} \eta_{ijk} \right\}, \quad (9)$$

where  $\delta_{u,u'}$  is the Kronecker delta,  $\tau_{ijk}^2$  is a scale parameter,  $\boldsymbol{\theta}_{ijk} = (\theta_{ijk1}, \theta_{ijk2}, \dots, \theta_{ijkp_u})^\top$  a vector of lengthscales, and  $\eta_{ijk}$  is a nugget – all site-specific. Denote the set of hyperparameters of the  $ijk^{\text{th}}$  OSS as  $\boldsymbol{\phi}_{ijk} = \{\tau_{ijk}^2, \boldsymbol{\theta}_{ijk}, \eta_{ijk}\}$ , with indices following Eq. (8).

To offer some visual contrast between these fits, Figure 1 shows the site-wise noise level

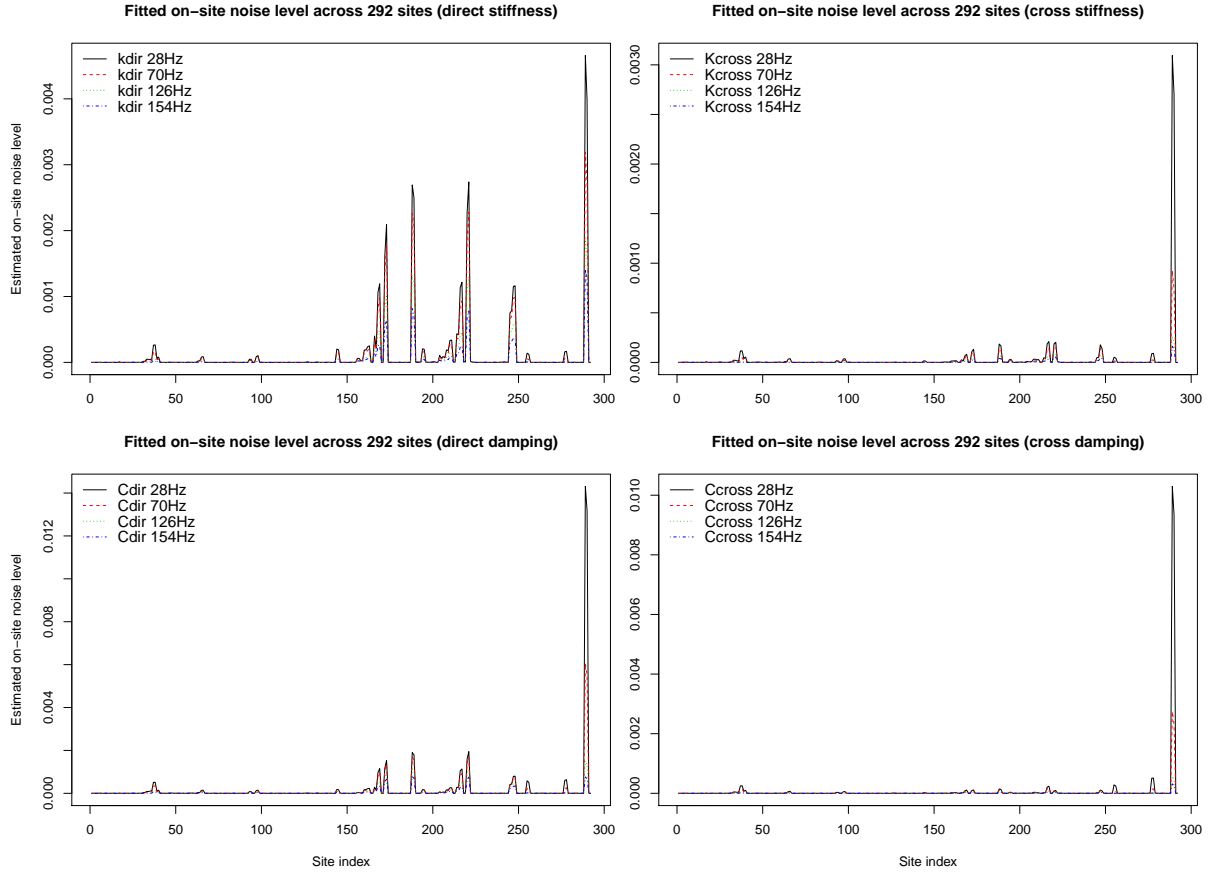


Figure 1: Univariate OSS noise levels represented by the trained  $\hat{\tau}_{ijk}^2 \hat{\eta}_{ijk}$  for direct/cross stiffness and damping at each of the four frequencies.

$\hat{\tau}_{ijk}^2 \hat{\eta}_{ijk}$  across the  $N_F = 292$  sites for the sixteen outputs. These are clearly non-constant, a testament to the nonstationary nature of OSSs across the input space represented by the 292  $\mathbf{x}_i$  settings, but also highly consistent across outputs at each frequency level. This suggests that a certain amount of information in each frequency is redundant. Although somewhat less obvious at first glance, notice that the overall noise level decreases as the frequency increases. The amount by which noise level drops depends on the input location, suggesting there is novel information in each output frequency, which might manifest as spatial dependency, albeit in a large ( $p_x = 17d$ ) space.

Before inserting these  $292 \times 16 = 4,672$  OSSs into the KOH apparatus for calibration, we performed an hyperparameter stability and predictive accuracy check on a commensurately

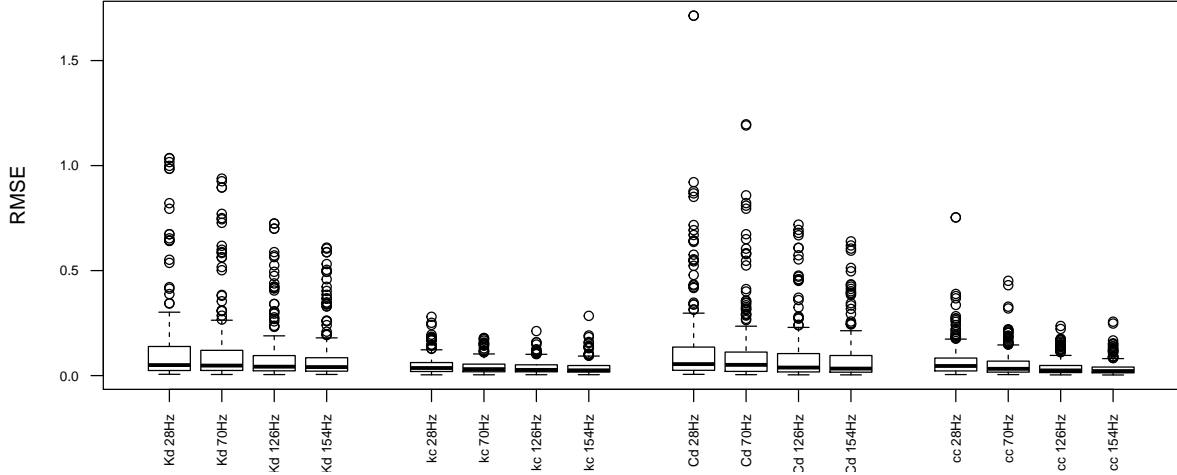


Figure 2: Boxplots of 292 out-of-sample root mean-squared errors (RMSEs).

sized out-of-sample on-site testing data set, again sixteen-fold across 1,672,000 **ISOTSEAL** runs. The hyperparameters looked similar to Figure 1, and are not shown here to save space. Prediction accuracies are summarized in Figure 2. Each boxplot collects the 292 on-site root mean-squared errors (RMSEs) from the  $n_{ijk} \approx 1,000$  converged runs on site  $i$ , separately for output  $j$  and frequency  $k$ . Observe that most OSSs ( $> 50\%$  via the median lines in the boxplots) act as interpolators on the sites, giving RMSEs are close to zero. The rest act as extrapolators or smoothers, with a small handful ( $\approx 5\%$  outside the whiskers) extremely so. Also notice that the scales of RMSEs consistently decrease as frequency increases, coinciding with the in-sample pattern(s) observed in Figure 1.

### 3.3 Challenges from univariate OSSs calibration

Next, combining with field data, we performed separate OSS-based fully Bayesian calibrations for  $\mathbf{u}$ , repeating the Huang et al. univariate approach for each output and frequency. I.e., we performed  $4 \times 4 = 16$  MCMCs, 100,000 samples each, and discarded 5,000 as burn-in. Each MCMC run took about three days to finish, after a warm start from modular optimization. To demonstrate the drawbacks from this univariate approach, Figures 3 and 4 present two views into the posteriors for  $\mathbf{u}_{jk}$ .

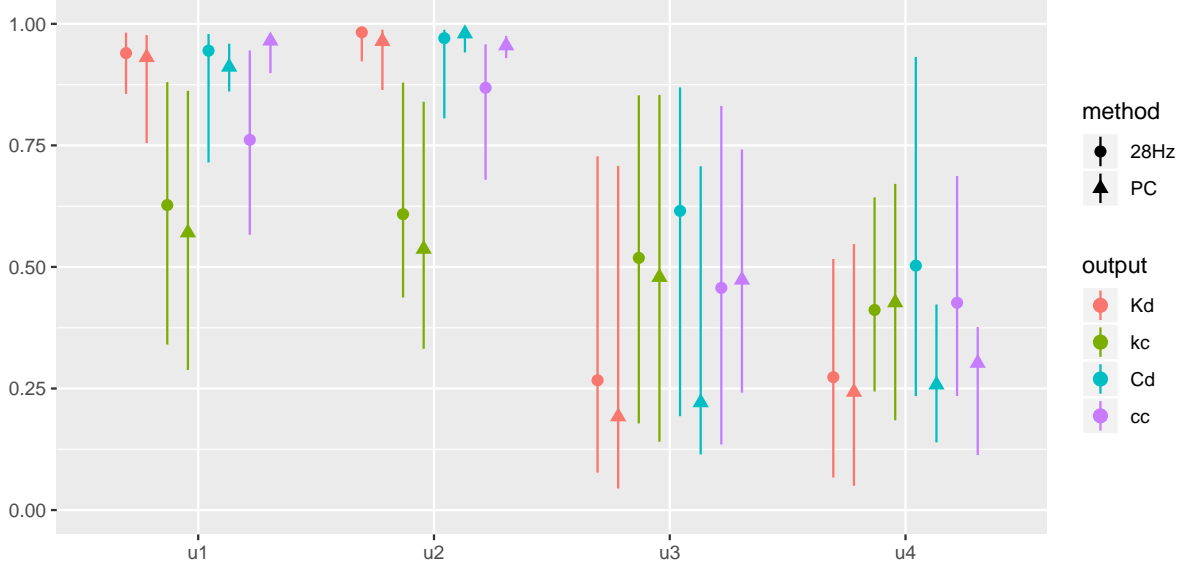


Figure 3: Marginal posterior distributions of  $\mathbf{u}$  from outputs  $K_d$ ,  $k_c$ ,  $C_d$ , and  $c_c$  at 28Hz (circles) and via principal components combining all output frequencies (triangles, Section 4.3). Dots indicate MAP values and error bars form 90% credible intervals.

Figure 3 shows marginal posteriors for the components of  $\mathbf{u}_{jk}$  for each output at 28Hz ( $k = 1$ ). The other frequencies, provided in Appendix A.1, look similar. To support a comparison coming later in Section 4.3, the plot also shows results combining all frequencies which will be discussed in due course. Focusing on the 28Hz results, notice that while some coordinates, like  $u_3$  and  $u_4$ , exhibit consistency in the high overlap of their credible intervals, others like  $u_1$  and  $u_2$  do not. There would appear to be complimentary (unused) information in these independent analyses. For a slightly higher resolution view, Figure 4 shows posteriors for pairs  $u_1 \times u_2$  for each output (at 28Hz) across the top, and  $u_3 \times u_4$  across the bottom. Again, the set of similar visuals is completed in the appendix. In the top row,  $k_c$  stands out as the exception. Despite wider credible regions in the bottom row, only one pair ( $k_c, c_c$ ) among the six resemble one another.

Taken together – and even for just these four sets of  $\mathbf{u}_{jk}$  posteriors, ignoring the other output frequencies — there is no way to stack them together in the 4-dimensional space to generate one single, concentrated solution with appropriate evaluation of individual parameter uncertainty from different outputs. These separately sampled  $\mathbf{u}_{jk}$  posteriors indicate

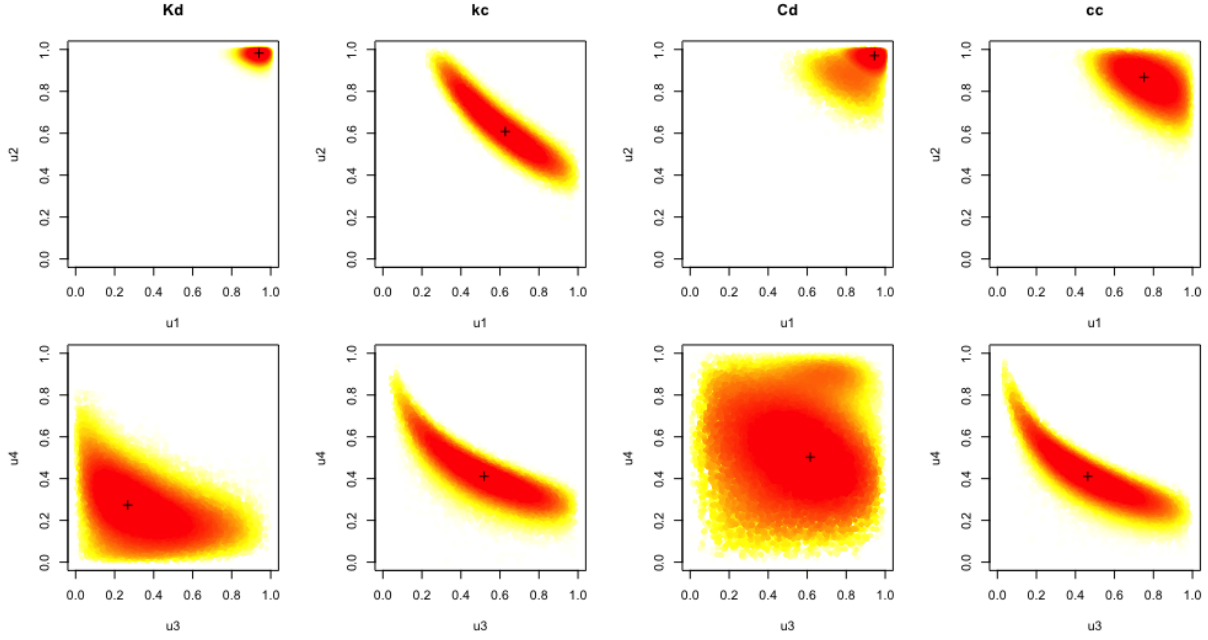


Figure 4: Bivariate marginal plots of single-output posterior samples of  $\mathbf{u}$  from outputs  $K_d, k_c, C_d$ , and  $c_c$  at 28 Hz. Dots are 100,000 MCMC samples of  $\mathbf{u}$ , heat colored according to the rank of (log) posterior probability. The “+” indicates the MAP values.

heterogeneity in parameter learning with varied amount of uncertainty, creating more uncertainty downstream to any engineering decision-making. A joint analysis not only holds the potential to reconcile (at times) contradictory information, but would also drastically simplify downstream decision-making with far fewer posterior views to scrutinize.

## 4 On-site surrogates with basis representation

The essential insight behind OSS-based calibration is that learning for  $\mathbf{u}$  is primarily driven by model discrepancy  $b(\mathbf{x})$ , which can only be observed at field input sites  $\mathbf{X}_{N_F}$ , through residuals. At a conceptual level, extending that to multivariate output is as simple as making the relevant quantities bold:  $\mathbf{y}_{ijk}^F(\mathbf{X}_{N_F})$  in the field and  $\hat{\mathbf{y}}_{ijk}^M(\mathbf{X}_{N_F}, \mathbf{U}_i)$  for the surrogate, and then calculating discrepancies with extra indices.

$$y_{ijk}^F(\mathbf{X}_{N_F}) - \hat{y}_{ijk}^M(\mathbf{X}_{N_F}, \mathbf{U}_i), \quad i = 1, 2, \dots, N_F, \quad j = 1, 2, \dots, J, \quad k = 1, 2, \dots, K. \quad (10)$$

As in the previous, univariate output setting, as long as the surrogate is good at those locations, which OSSs facilitate, further considerations can be pushed downstream. For example, when new locations are of interest, say for prediction, new OSSs/runs can be built/Performed there, which is trivial if (like **ISOTSEAL**) the simulations are fast.

The devil is, however, in the details for how these residuals (10) are modeled. Section 3.3 demonstrates that separating over  $j$  and  $k$  for the honeycomb leads to pathologies. Here we begin the description for a joint analysis, building a fitted bias for residuals all at once, to resolve those inconsistencies while ensuring that all relevant information is incorporated in posterior inference for  $\mathbf{u}$ , thus filtering to downstream tasks like prediction. What we propose below is customized, to a degree, to the honeycomb setting, e.g., via fixed  $j$  (output classes) and pooling over  $k$  (output frequencies) in Eq. (10). Completing the description by combining over output classes (pooling over  $j$ ) is deferred to Section 5. This partition works well because of the nature of similarities in OSSs demonstrated in Section 3.2. We begin here with some notational setup that applies for all  $j$  and  $k$ , and then fix  $j$  for the remainder of the section. Although we believe other applications – perhaps with more or fewer indices – could be set similarly, further speculation is left to Section 6.

Let  $\mathbf{Y}_i^M(\mathbf{U}) = [\mathbf{y}_{i11}^M(\mathbf{U}_i), \mathbf{y}_{i12}^M(\mathbf{U}_i), \dots, \mathbf{y}_{i44}^M(\mathbf{U}_i)]$ , for  $i = 1, 2, \dots, N_F$ , be a 16-column matrix (four outputs at four frequencies) holding the  $n_i \approx 1000$  rows of converged **ISOTSEAL** runs for the  $i^{\text{th}}$  site. Now collect  $N_F = 292$  of these  $\mathbf{Y}_i^M(\mathbf{U})$

$$\begin{aligned} \mathbf{Y}^M(\mathbf{U}) &= [\mathbf{Y}_1^M(\mathbf{U})^\top, \mathbf{Y}_2^M(\mathbf{U})^\top, \dots, \mathbf{Y}_{N_F}^M(\mathbf{U})^\top]^\top & (11) \\ &= \begin{bmatrix} \mathbf{y}_{111}^M(\mathbf{U}_1) & \mathbf{y}_{112}^M(\mathbf{U}_1) & \dots & \mathbf{y}_{144}^M(\mathbf{U}_1) \\ \mathbf{y}_{211}^M(\mathbf{U}_2) & \mathbf{y}_{212}^M(\mathbf{U}_2) & \dots & \mathbf{y}_{244}^M(\mathbf{U}_2) \\ \vdots & \vdots & \vdots & \vdots \\ \mathbf{y}_{N_F11}^M(\mathbf{U}_{N_F}) & \mathbf{y}_{N_F12}^M(\mathbf{U}_{N_F}) & \dots & \mathbf{y}_{N_F44}^M(\mathbf{U}_{N_F}) \end{bmatrix}_{N_M \times 16} \end{aligned}$$

whose row dimension is  $N_M = \sum_{i=1}^{N_F} n_i = 286,282$ . Recall that  $\mathbf{U}_i$  are  $n_i \times p_u$  on-site

(maximin LHS) design matrices.

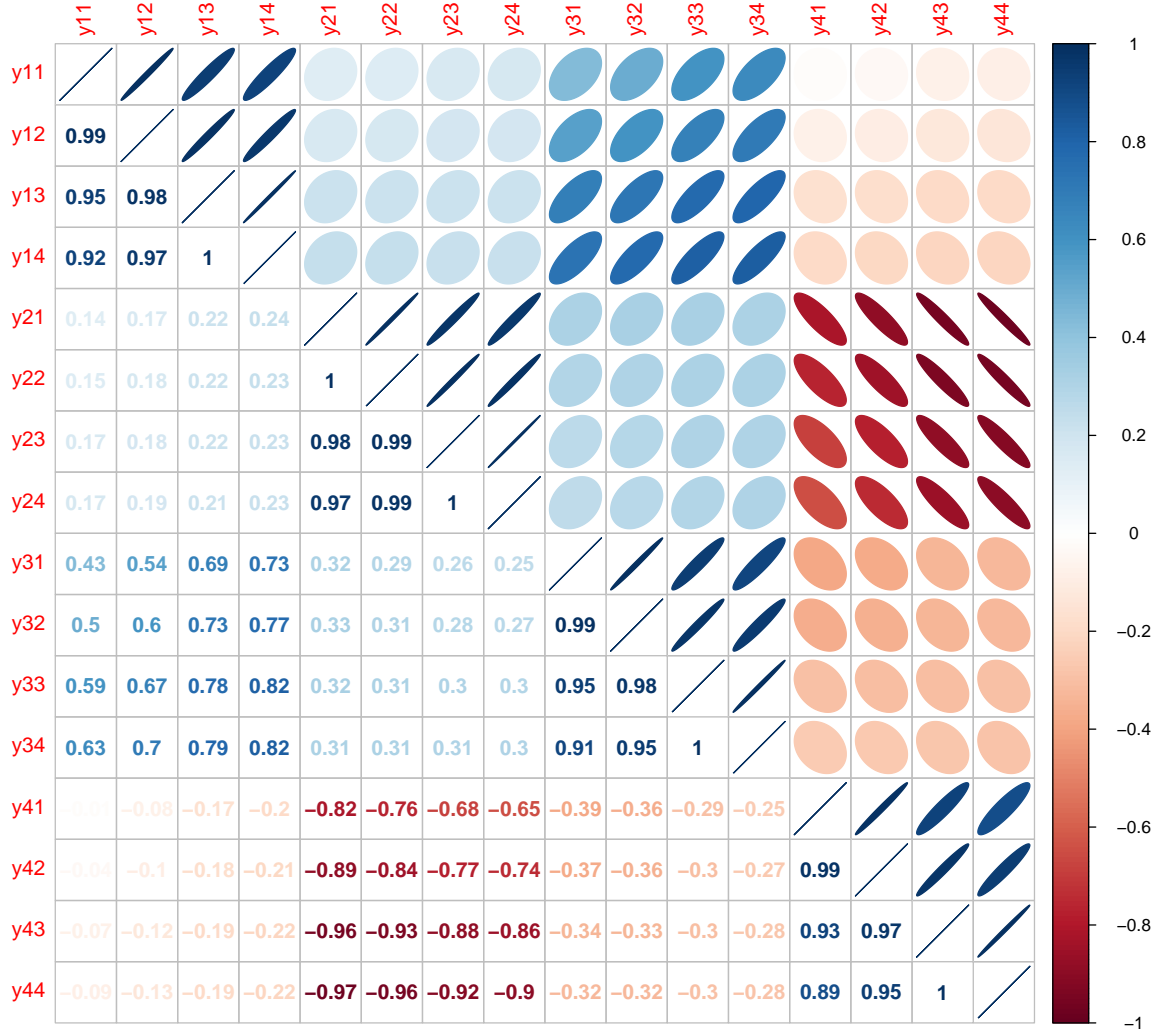


Figure 5: Correlation matrix (number in lower triangle and ellipse in upper triangle) of  $N_M = 286,282$  multivariate ISOTSEAL simulation of direct/cross stiffness and damping at frequencies 28, 70, 126, and 154 Hz. In the output labels  $y_{jk}$ ,  $j = 1, \dots, 4$  for output property and  $k = 1, \dots, 4$  for frequency, as defined in Eq. (8).

We performed an initial exploratory data analysis (EDA) with these data, one aspect of which is  $\text{Cor}\{\mathbf{Y}^M(\mathbf{U})\}$ , visualized in Figure 5. Correlation strength and association is indicated numerically in the lower-triangle, by elliptical shape and direction in the upper half, and by color and shading in both. Four-by-four blocks are clearly evident in this view, indicating strong linear correlation between different frequency levels within the same property (block of) output, but weaker correlation between types. Our EDA also revealed

similar correlations exhibited by the output-combined field data  $\mathbf{Y}^F$ , defined similarly. This is not shown here for brevity. Taken together, we conclude that parsimonious representation of across-frequency information could be beneficial to a joint modeling enterprise.

## 4.1 Principal component OSSs

We propose performing principal component analysis (PCA) across frequency outputs in an “on-site” fashion, i.e., fit a PC basis in the subspace spanned by  $\mathbf{U}_i, i = 1, \dots, N_F$  on the  $N_F$  observed physical sites  $\mathbf{X}_{N_F}$  for each type (block, indexed by  $j$ ) of outputs. Fixing  $j$ , we first center and standardize the correlated  $K = 4$  frequencies, perform PCA on the  $N_M \times K$  dimensional “on-site” matrix,

$$\mathbb{PC}\{\mathbf{Y}_j^F - \mathbf{Y}_j^M\}, \quad \text{yielding eigenvectors } \mathbf{W}_j, \quad \text{for } j = 1, \dots, J. \quad (12)$$

In Eq. (12),  $\mathbf{Y}_j^F$  collects  $K = 4$  columns of  $n_i$ -row replicated field outputs across frequencies,

$$\mathbf{Y}_j^F = \begin{bmatrix} \mathbf{y}_{1j1}^F & \mathbf{y}_{1j2}^F & \mathbf{y}_{1j3}^F & \mathbf{y}_{1j4}^F \\ \mathbf{y}_{2j1}^F & \mathbf{y}_{2j2}^F & \mathbf{y}_{2j3}^F & \mathbf{y}_{2j4}^F \\ \vdots & \vdots & \vdots & \vdots \\ \mathbf{y}_{N_F j 1}^F & \mathbf{y}_{N_F j 2}^F & \mathbf{y}_{N_F j 3}^F & \mathbf{y}_{N_F j 4}^F \end{bmatrix}_{N_M \times 4}, \quad (13)$$

where  $\mathbf{y}_{ijk}^F \equiv (y_{ijk}^F(\mathbf{x}_i), \dots, y_{ijk}^F(\mathbf{x}_i))^\top$  is the  $n_i$ -time replicated field output  $y_{ijk}^F(\mathbf{x}_i)$  on  $i^{\text{th}}$  site for output  $j$  at frequency  $k$ . Similarly,  $\mathbf{Y}_j^M$  collects  $K = 4$  columns of on-site ISOTSEAL simulations on  $N_F$  sites at multiple frequencies provided in Eq. (11).

For honeycomb, there are  $J = 4$  properties (blocks):  $\{K_d, k_c, C_d, c_c\}$ . Thus, we performed four separate PCAs in total. Figure 6 summarizes these via scree plots of variance decomposition, accompanied by a table with a numerical summary via the top variances. Notice that the first PCs dominate in all four cases. Output  $c_c$  which might

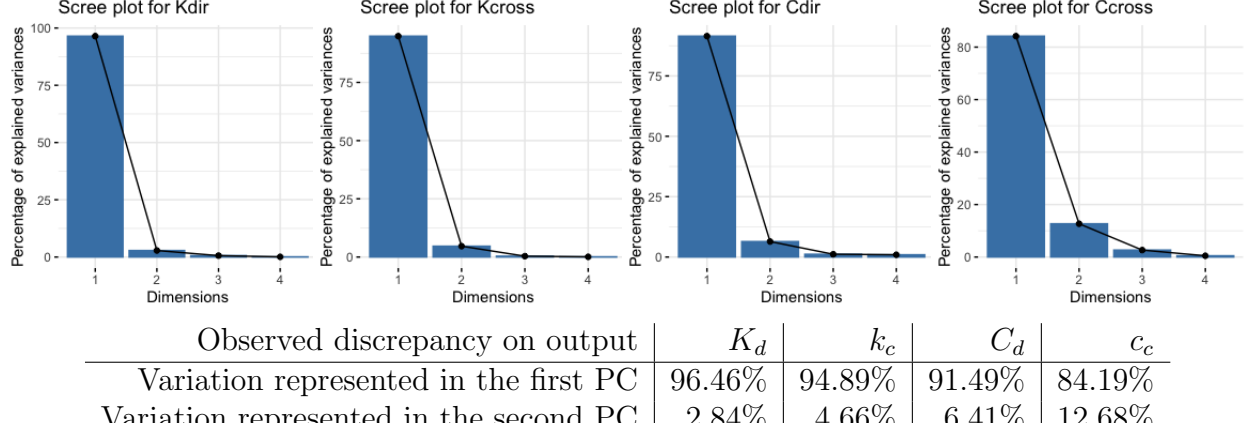


Figure 6: Scree plots and tabulation of PCA variances.

marginally benefit from the second principal direction.

This suggests that a Higdon et al. (2008)-style basis-based-surrogate (6), projecting down to one principal direction for these four outputs (separately over output property  $j$ ) could be effective here, after upgrading to accommodate OSSs. Instead of breaking down the simulator and discrepancies into two separate principal representations in (6), we prefer a single PCA through the matrix of eigenvectors  $\mathbf{W}_j$  trained from the whole “on-site” observed discrepancy in (12). In particular, we use the first (column) eigenvector  $\mathbf{w}_j^1$  of  $\mathbf{W}_j$  to extract the first PCs from multiple frequency outputs of both simulated  $\mathbf{y}_j^{M1} = \mathbf{Y}_j^M \mathbf{w}_j^1$  and field  $\mathbf{y}_j^{F1} = \mathbf{Y}_j^F \mathbf{w}_j^1$ . Once extracted, we can put them together as

$$\mathbf{y}_j^{F1}(\mathbf{x}) = \mathbf{y}_j^{M1}(\mathbf{x}, \mathbf{u}^{*1}) + \mathbf{b}_j^1(\mathbf{x}) + \epsilon_j^1. \quad (14)$$

which may be interpreted as ordinary KOH in the first PC subspace. Observe the introduction of new notation for model discrepancy  $\mathbf{b}_j^1(\mathbf{x})$ , best calibration setting  $\mathbf{u}^{*1}$ , and iid noise  $\epsilon_j^1$ , to recognize PC pre-processing to form  $\mathbf{y}_j^{F1}(\mathbf{x})$  and  $\mathbf{y}_j^{M1}$ . Focus remains on observed sites only, i.e.,  $\mathbf{x} \equiv \mathbf{X}_F$  in the on-site setting, for observed discrepancies, and surrogate(s) trained on  $N_M = 286,282$  dense paired with space-filling  $\mathbf{U}_i$ ’s. After learning, prediction, etc., may be linearly back-transformed to the original full space.

## 4.2 PC-level OSSs calibration: optimization and full Bayes

Each first on-site PC can be used in a separate calibration: four this time instead of sixteen in Section 3.3. Though plug-n-play, yielding improved  $\mathbf{u}_j$  posteriors as we shall demonstrate momentarily, the result(s) are somewhat underwhelming. Here we illustrate how these on-site basis representations may be plugged into the OSS calibration framework as an intermediate step toward a fully joint model (all sixteen) in Section 5.

**Modular calibration via optimization.** Here the goal is to search for  $\hat{\mathbf{u}}_j^1$  by maximizing the posterior probability of (observed) model discrepancy (4) in the first principal direction. Update Eq. (4) by swapping the univariate (column vector) observed discrepancy with that based on first eigenvector  $\mathbf{w}_j^1$  obtained in Eq. (12). I.e., for each of  $j = 1, \dots, J$ ,

$$\mathbf{D}_{N_F}^B(\mathbf{u}) = (\mathbf{X}_{N_F}^F, \mathbf{y}_{N_F}^F - \hat{\mathbf{y}}_{N_F}^M(\mathbf{u})) \rightarrow \mathbf{D}_{N_F}^{j1}(\mathbf{u}_j^1) = (\mathbf{X}_{N_F}^F, (\mathbf{Y}_j^F - \hat{\mathbf{Y}}_j^M(\mathbf{u}_j^1))\mathbf{w}_j^1), \quad (15)$$

In (15),  $\mathbf{Y}_j^F$  is fixed and  $\hat{\mathbf{Y}}_j^M(\mathbf{u}_j^1)$  are OSS [fitted as in Section 3.2] evaluations at  $\mathbf{u}_j^1$ , which would vary along a numerical optimizer's search trajectory. The mathematical program(s), defining objective(s) implicitly, are identical to Eq. (4) but with  $\mathbf{D}_{N_F}^B(\mathbf{u}) \rightarrow \mathbf{D}_{N_F}^{j1}(\mathbf{u}_j^1)$  and  $\phi \rightarrow \phi_j^1$  denoting hyperparameters involved in each of  $j$  GP-based fitted discrepancies.

**Bayesian joint inference.** Posterior sampling of  $\mathbf{u}_j^1$  requires projecting  $\mathbf{Y}_j^F$  (13) and  $\mathbf{Y}_j^M$  (11) onto their first principal axis,  $\mathbf{y}_j^{F1}$  and  $\mathbf{y}_j^{M1}$  respectively, via Eq. (12). Then, following Eq. (14), one may impose a joint MVN (2), with mean zero and covariance  $\Sigma_j^1(\mathbf{u}_j^1)$ , whose structure is re-notated below with appropriate indices/first PC indicators:

$$\Sigma_j^1(\mathbf{u}_j^1) \equiv \begin{bmatrix} \Sigma_{N_M}^{j1} & \Sigma_{N_F, N_M}^{j1}(\mathbf{u}_j^1)^\top \\ \Sigma_{N_F, N_M}^{j1}(\mathbf{u}_j^1) & \Sigma_{N_F}^{j1}(\mathbf{u}_j^1) + \Sigma_b^{j1} \end{bmatrix}. \quad (16)$$

Posterior evaluation for  $\mathbf{u}_j^1$  in a Metropolis setting requires decomposing this  $\Sigma_j^1(\mathbf{u}_j^1)$  for inverse and determinant components of the MVN log likelihood. Note the size of this matrix is  $(N_M + N_F)^2$ , where  $N_M + N_F = 286,574$  for our honeycomb application. Consequently, ordinary cubic in  $(N_M + N_F)$  decomposition costs pose a serious bottleneck.

Fortunately,  $\Sigma_j^1(\mathbf{u}_j^1)$  has a convenient structured-sparsity form under OSSs. Here we extend Huang et al. (2020) to describe the composition of non-zero blocks of this matrix for first PCs (12). The largest block  $\Sigma_{N_M}^{j1}$ , corresponding to the OSSs themselves, is the most sparse. In fact, it is block-diagonal with  $N_F$  blocks:  $\Sigma_{N_M}^{j1} = \text{Diag}[\Sigma_i^{j1}(\mathbf{U}_i, \mathbf{U}_i)]$ . Each block  $\Sigma_i^{j1}(\mathbf{U}_i, \mathbf{U}_i)$  may be built from the kernel of the  $i^{\text{th}}$  OSS conditioned on any fitted hyperparameters from  $\mathbf{y}_{ij}^{M1}$ . Since it does not depend on  $\mathbf{u}_j^1$ , each may be pre-decomposed separately at manageable  $\mathcal{O}(n_i^3)$  cost.

The rest of  $\Sigma_j^1(\mathbf{u}_j^1)$  requires bespoke construction given novel  $\mathbf{u}_j^1$ , but still has convenient block-sparse structure. The simulator-field cross covariance piece is block-diagonal,  $\Sigma_{N_F, N_M}^{j1}(\mathbf{u}_j^1) = \text{Diag}[\Sigma_i^{j1}(\mathbf{u}_j^1, \mathbf{U}_i)]$ , where  $\Sigma_i^{j1}(\mathbf{u}_j^1, \mathbf{U}_i)$  is a row vector of site-wise covariance between calibration inputs  $\mathbf{u}_j^1$  and on-site design matrix  $\mathbf{U}_i$ . Finally, although  $\Sigma_{N_F}^{j1}(\mathbf{u}_j^1) + \Sigma_b^{j1}$  is dense, it is small ( $N_F \times N_F$ ) and thus cheap to decompose. The first component  $\Sigma_{N_F}^{j1}(\mathbf{u}_j^1)$  is block diagonal, where each block is like  $\Sigma_i^{j1}(\mathbf{U}_i, \mathbf{U}_i)$  from the  $i^{\text{th}}$  OSS kernel, except with a stacked  $\mathbf{u}_j^1$  vectors in lieu of the  $\mathbf{U}_i$ . The second component  $\Sigma_b^{j1}$  is dense and comes from the discrepancy kernel using all field-data inputs. Any hyperparameters, e.g.,  $\hat{\phi}_j^1$  are most easily set via maximization-based pre-analysis, e.g., following Eq. (15), but could also be included in the MCMC.

Once  $\Sigma_j^1(\mathbf{u}_j^1)$  in Eq. (16) is built, for each proposed  $\mathbf{u}_j^1$  setting in a Metropolis scheme, and after its component parts have been decomposed, a full decomposition – i.e., combining from constituent parts – involves tedious but ultimately straightforward matrix multiplication via partition inverse and determinant equations (e.g., Petersen and Pedersen, 2008), of course skipping any multiply-by-zeros. The details are similar to Section 4.2 of Huang et al. (2020), and so are not repeated here.

### 4.3 PC-level calibration results

Isolating each  $\{K_d, k_c, C_d, c_c\}$ , but leveraging strong linear correlation across frequencies ( $4 \times 4 = 16$  total outputs), eliminates redundant information and brings the unit of analysis down fourfold to 4. The computational merits of OSSs, ported to a PC basis, enables efficient modular optimization and fully Bayes inference on parameter(s)  $\mathbf{u}_j^1$ . Here we present the outcome of such analysis with an eye toward a fully combined setup in Section 5. We focus on contrasting to two earlier views, from a fully independent, separated (16-fold) analysis provided in Section 3.1.

Figure 3 shows 1d posterior marginals for  $\mathbf{u}_j^1$ , for each  $j = 1, \dots, 4$ , alongside their 28Hz-only analog. With four coordinates of  $\mathbf{u}$ , a total of sixteen comparisons may be made with this view. Observe, for example, that  $u_1, u_2$ , and  $u_4$  show considerable concentration of density under PC for outputs  $C_d$  and  $c_c$ . There is also a considerable shift in the location of posterior mass (i.e., the MAP), with  $u_1$  and  $u_2$  shifting up and  $u_4$  shifting down for  $c_c$ . The rest of the PC marginals are similar to their 28Hz counterparts.

Figure 7 offers a similar comparison in 2d when contrasted with Figure 4 in Section 3.1. As in that view, only a subset of pairs of outputs are shown. The rest are in Appendix A.2. Notice the marked improvement in posterior concentration in the rightmost four panels. Two of those panels,  $(u_3 \times u_4)$  for  $C_d$  and  $(u_1, u_2)$  for  $c_c$ , also show substantial re-location of density compared to their 28Hz analog. The leftmost four panels offer less stark contrast, a view shared by the 1d analysis in Figure 3.

These results indicate that we are headed in the right direction. We embarked on this analysis knowing well that the diversity of information across output frequencies would not be substantial. Nevertheless, representing it in a parsimonious way, through first PCs, seems to enhance posterior concentration even though data is being discarded (i.e., the other three PCs). This is a hallmark of enhanced learning through dimension reduction. The last step is to combine these separate analyses into one, forming a posterior for a single

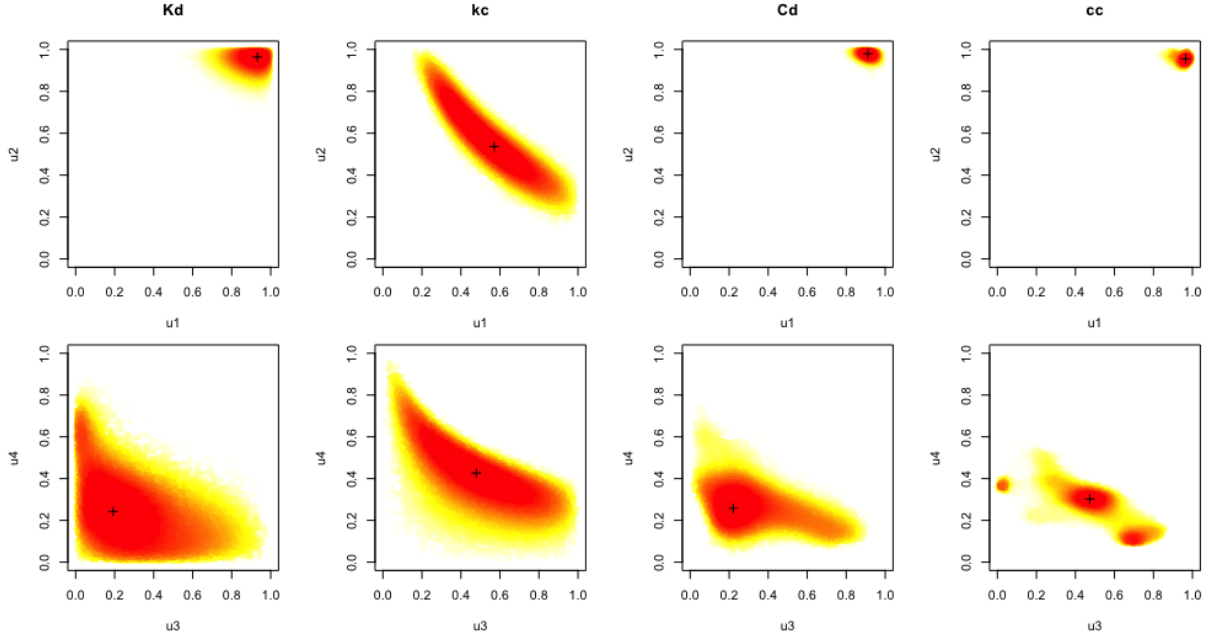


Figure 7: Bivariate marginal plots of posterior samples of  $\mathbf{u}_j^1$  from PC-combined outputs  $K_d, k_c, C_d$ , and  $c_c$ . Dots are 100,000 MCMC samples of  $\mathbf{u}_j^1$ , heat colored according to the rank of (log) posterior probability. The “+” indicates the MAP values.

set of unknowns given the entirety of data on all simulation and field outputs.

## 5 Full integration of outputs

The final step in our analysis is, in some sense, the easiest – that is, once all the hard work of building OSSs, forming first-PC posteriors, etc., is done. After detailing how outputs  $j = 1, \dots, J$  may be combined, we provide a final suite of views into a unified posterior for  $\mathbf{u}^1$ . Although the setup is rather generic in  $j$ , in what follows we continue to focus the discussion on the honeycomb application in anticipation of those results.

### 5.1 Inferential apparatus

Section 4.1 demonstrated that a PC basis is effective as a dimension reduction tool for four pairs of four honeycomb output frequencies. Those four bases, calculated separately but combined momentarily, captures around a  $4 \times 90\% \approx 360\%$ -fold higher degree multivariate

variability as compared to each single univariate output. On the other hand, each output property  $j$  (direct/cross stiffness or damping) has a distinct physical meaning, and the dependence between them is highly non-linear.<sup>1</sup> In Figure 5 we saw no evidence of strong linear dependence across the  $J = 4$  output classes, which nudged us toward an independence assumption into this joint analysis. We shall return to that in our discussion in Section 6.

As a related, but ultimately practical matter, each output is measured in very different units/scales. However, PCA helps here. Standardization of the 16d raw outputs, as a pre-processing step, followed by orthogonal projection onto the 4-column subspaces spanned by their first eigenvectors  $\mathbf{w}_j^1$ , naturally place those quantities on an equal footing. Besides being represented in the direction of highest variability, they are also scale-free which simplifies joint modeling downstream.

**Modular calibration via optimization.** Recall that each OSS, i.e.,  $N_F \times J \times K = 4,672$  univariate fits [Section 3.2] involves a manageable  $\mathcal{O}(n_i^3)$  calculation. Then each of  $K = 4$  output frequencies are combined into their first PC (12). Finally, combine these representations together into a unified objective to obtain a single  $\mathbf{u}^1$  under Eq. (4) for all ( $J = 4$ ) observed discrepancies, with modular inference for GP hyperparameters  $\phi_j^1$  in each subspace. So basically we wish to combine multiple Eq. (4) for a single  $\mathbf{u}^1$  via  $\mathbf{D}_{N_F}^{j1}(\mathbf{u}_j^1) = (\mathbf{X}_{N_F}^F, (\mathbf{Y}_j^F - \hat{\mathbf{Y}}_j^M(\mathbf{u}_j^1))\mathbf{w}_j^1)$ , for  $j = 1, \dots, J$ . After imposing conditional independence given common  $\mathbf{u}^1$ , the following objective is immediate:

$$\hat{\mathbf{u}}^1 = \arg \max_{\mathbf{u}^1} \left\{ p(\mathbf{u}^1) \prod_{i=1}^J \left[ \max_{\phi_j^1} p_b(\phi_j^1 \mid \mathbf{D}_{N_F}^{j1}(\mathbf{u}^1)) \right] \right\}. \quad (17)$$

In practice, of course, it easiest to solve this in log space. For each value of  $\mathbf{u}^1$  entertained by a numerical optimizer, evaluation requires GP fitting for  $J = 4$  observed discrepancies  $\mathbf{D}_{N_F}^{j1}(\mathbf{u}_j^1)$ , each with  $\hat{\phi}_j^1$  offloaded to a separate, library-facilitated, numerical optimizer.

---

<sup>1</sup>This is quite different from the linear form of the differential equation linking them (7).

To leverage ubiquitous modern multi-core workstation resources, we fit these in parallel. Following Huang et al. (2020), as with all other such optimisations in this manuscript, BFGS for  $\hat{\mathbf{u}}^1$  via `nloptr` in R wrapped in a multi-start scheme facilitates a simple implementation.

**Bayesian joint inference.** Posterior sampling  $\mathbf{u}^1$  may follow similar principals. With the  $j^{\text{th}}$  output in first-PC representation, i.e.,  $\mathbf{y}_j^{F1}$  and  $\mathbf{y}_j^{M1}$  via Eq. (12), a joint posterior via conditional independence follows from a likelihood in product form:

$$p(\mathbf{u}^1 \mid \mathbf{y}_1^{F1}, \mathbf{y}_1^{M1}, \dots, \mathbf{y}_J^{F1}, \mathbf{y}_J^{M1}) \propto p(\mathbf{u}^1) \cdot \prod_{i=1}^J p(\mathbf{y}_j^{F1}, \mathbf{y}_j^{M1} \mid \mathbf{u}^1). \quad (18)$$

Under the multivariate OSSs emulation structure, Metropolis rejection for  $\mathbf{u}^1$  can be broken down to evaluation of each (log) MVN-likelihood,  $p(\mathbf{y}_j^{F1}, \mathbf{y}_j^{M1} \mid \mathbf{u}^1)$ , for  $j = 1, \dots, J$ . Again, each may be performed in parallel. As they are identically sized, this makes for a nice “data-parallel” implementation across  $j$  via partition input equations on block-sparse  $\Sigma_j^1(\mathbf{u}_j^1)$ . A modular optimization solution (17) can provide a warm-start to minimize burn-in efforts.

## 5.2 Joint results

Here we present views into our fully integrated calibration results. Our modular optimization(s) utilized a 500-random-multi-start BFGS implemented in parallel. Although more time is required for jointly optimizing four separate sub-objectives at each iteration, the overall waiting time for joint optimization turns out to be comparable to univariate and PC-based variations. A post-optimization analysis summarizes the median number of `nloptr` iterations until convergence for each methods from 500 random initialization: 335 for PC- $K_d$ , 114 for PC- $k_c$ , 552 for PC- $C_d$ , 430 for PC- $c_c$ , and 117 for the unified approach. Speed of the unified approach may owe to the flatter/smooth surface, shown momentarily. For full Bayes via MCMC, the running time is also comparable to its univariate and PC counterparts, thanks to the multiple, and highly parallelizable, and sparse OSS covariance.

Figure 8 provides a 2d look via full posterior (bottom-left triangle) and multi-start optimization (top-right) and univariate marginals (diagonal). This may be contrasted with any of the PC-level analogues in Appendix A.2 to reveal how information is synthesized across outputs in this joint analysis. While the optimized solutions demonstrate how lo-

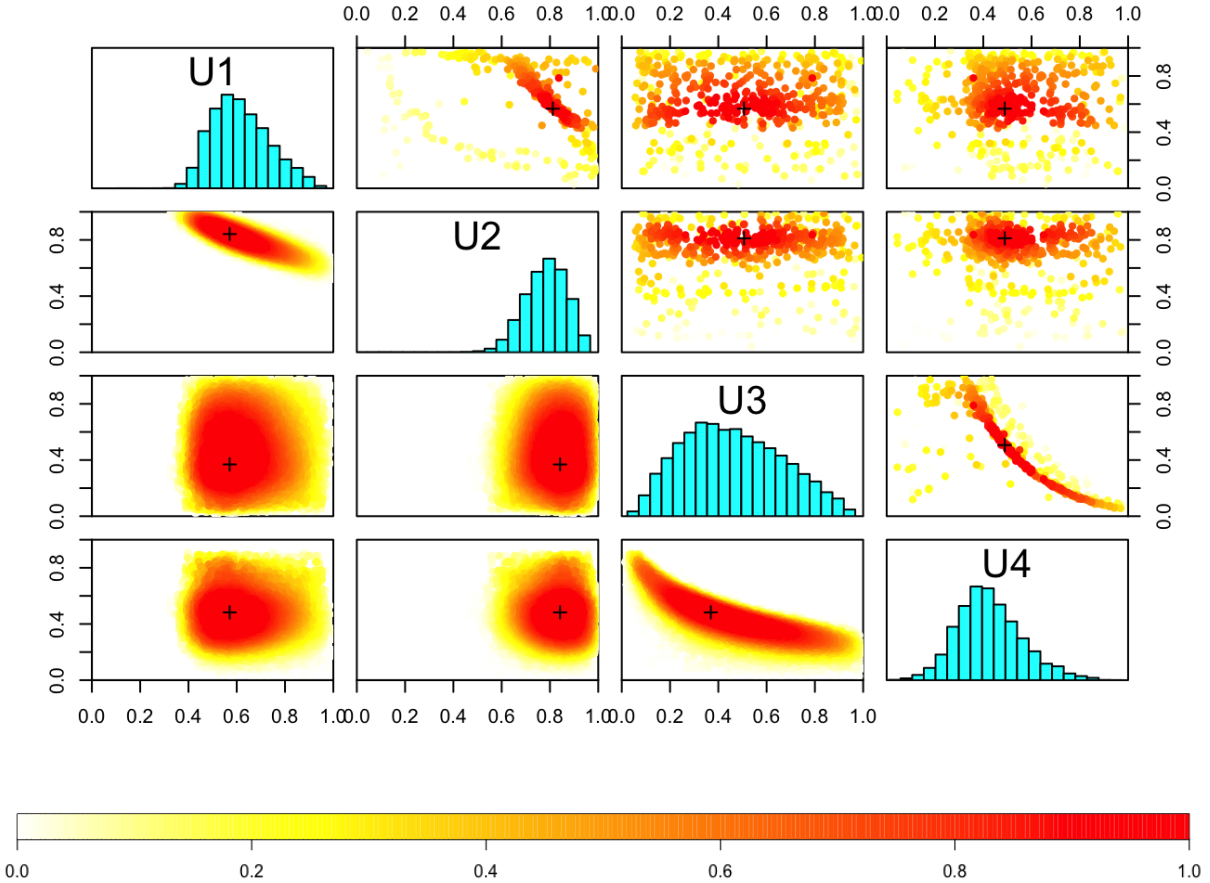


Figure 8: Fully Bayesian (lower and diagonal) and modular optimization (upper) calibration results for  $\mathbf{u}^1$  from the unified approach combining all 16 outputs. Heat color are derived from rank of (joint) log posterior probability of these parameter values. Bayesian results are from 100,000 MCMC samples after burn-in. Optimization results are from 500 converged optimization under random initialization. “+” signs indicate the MAP values.

cal dynamics challenge optimization, its MAP estimation and high density regions are comparable to the fully Bayesian ones. From both approaches, two dependent structures between pairs of parameter  $(u_1, u_2)$  and  $(u_3, u_4)$  can be observed, displaying an interesting relationship between the friction coefficients  $(u_1, u_2)$  and friction exponents  $(u_3, u_4)$ .

Our BHGE colleagues concluded that this pattern may be explained by an underlying turbulent-lubrication friction factor model from bulk-flow theory (Hirs, 1973).

Figure 9 is lower resolution, providing a 1d look, but allows a more visually immediate comparison. Here we see how each output property contributes to the final global solution

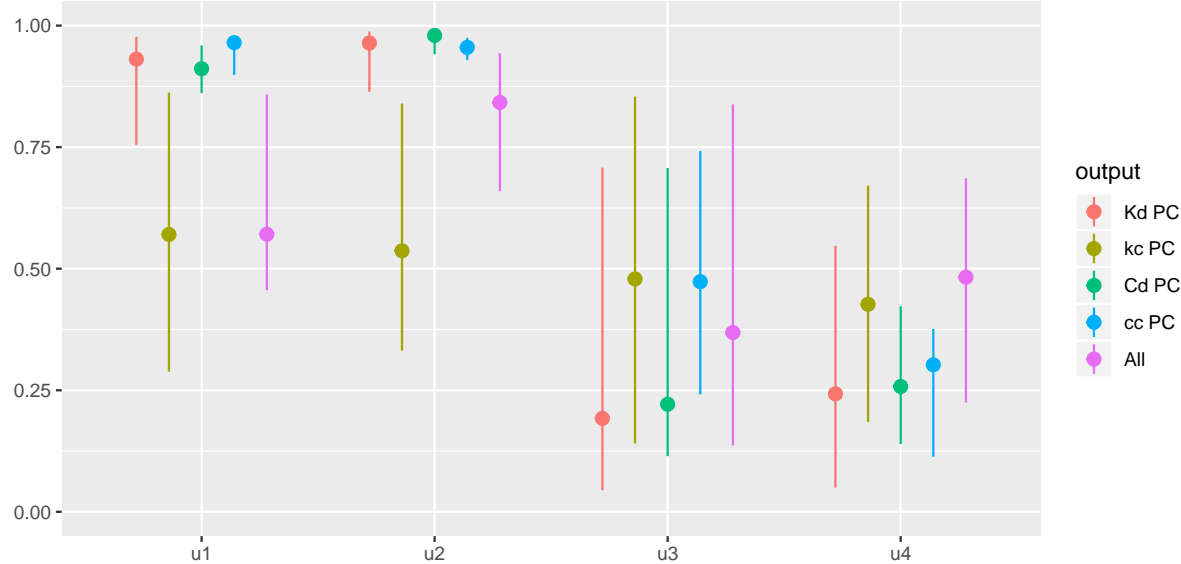


Figure 9: Side-by-side comparison between marginal posterior distributions of  $\mathbf{u}_j^1, j = 1, \dots, 4$  from outputs  $K_d, k_c, C_d$ , and  $c_c$  (labeled ‘PC’) and  $\mathbf{u}^1$  via unified output (labeled ‘All’). Dots indicate MAP values and error bars form 90% credible intervals.

$\mathbf{u}^1$ , with the output property. Apparently, cross stiffness ( $k_c$ ) is the most influential. Notice the similarity between the  $\mathbf{u}^1$  posterior distribution with  $k_c$  PC posterior  $\mathbf{u}_2^1$  in each of the  $u$  dimensions, especially in  $u_1$ . Further comparisons in 2d, via both the  $\mathbf{u}^1$  marginals in Figure 8 and PC-calibrated  $\mathbf{u}_2^1$  marginals shown in Figure 13 from Appendix A.2, demonstrate dependence in parameters ( $u_1, u_2$ ).

When comparing the landscape of solutions in upper triangle of Figure 8 with those from Figures 13–14 one immediately appreciates the benefit of a smoother posterior surface via full integration. Notice in those figures that the optimized solutions from outputs  $K_d$ ,  $k_c$  and  $C_d$  are quite concentrated in very small (dense red) peaks, in contrast to the much flatter surfaces from  $c_c$  [Figure 13] and the fully integrated [Figure 8]. The full Bayes (lower and diagonal) marginals further exhibit this pattern: fully integrated and PC- $c_c$  exhibit

flatter posteriors, with two ridges in  $(u_1, u_2)$  and  $(u_3, u_4)$ ; the other three PC-based results produce much narrower peaked posterior surfaces, specially in dimension of  $(u_1, u_2)$ .

## 6 Discussion

Motivated by a large-scale industrial multivariate calibration problem studding (honeycomb) seal flow dynamics from oil and gas research, we developed a new multivariate calibration method by extending a few features of a parsimonious univariate strategy based on on-site surrogates (OSSs; Huang et al., 2020). Tailored to effectively capture unique simulation features including high-dimensional input space, local nonstationary, missing simulations, and model fidelity at scale, this method is practical, but it is not without drawbacks. Univariate output applications, when replicated across diverse outputs are not immune to a data-poor Bayesian learning drawbacks for both high-dimensional calibration parameter and ill-posed model discrepancy. Our research began by exposing such drawbacks for the honeycomb.

Our solution, toward a multivariate OSS-based calibration, gathered together responses to several features of the honeycomb. A careful exploratory data analysis (EDA) suggested that a principal component-style basis representation could be effective for handing honeycombs quadruplet of highly linearly dependent output frequencies. We then update the OSS framework for both modular/optimized and fully Bayesian implementations PC-based calibration within the Kennedy & O'Hagan framework. Our empirical results indicated improved parameter identification and posterior concentration for calibration parameters, compared to the (separate) univariate analog. Then, we designed an independent multi-output PC approach to gather these models across output property. This was motivated by a lack of linear correlation observed in our EDA. The result is a unified analysis for the honeycomb, synthesizing millions of simulation runs in a matter of hours.

It might be possible to entertain nonlinear dependency among output properties, as

suggested by the differential equation (7) known to govern relationships across outputs of the types studied in honeycomb. On the other hand though, our visual inspections (via EDA) did not reveal any notable patters. So at this time, the merits of such an approach are speculative at best, although extension is certainly possible. We did not address prediction in this manuscript. Details are provided by Huang et al. (2020) in the univariate case. These are easy to extend to first PCs via  $\mathbf{u}_j^1$  with a similar MVN structure augmenting the two training data components (for simulation and field data) to predictive analogues, with the usual Gaussian process conditioning to form Kriging equations.

## Acknowledgments

Authors JH and RBG are grateful for support from National Science Foundation grants DMS-1521702 and DMS-1821258. JH and RBG also gratefully acknowledge funding from a DOE LAB 17-1697 via subaward from Argonne National Laboratory for SciDAC/DOE Office of Science ASCR and High Energy Physics. We thank Andrea Panizza (BHGE) for early work on this project, and for initiating the line of research, and Mirko Libraschi (BHGE) for many interesting discussions, and BHGE generally for being generous with their data, time, and expertise.

## References

Arendt, P. D., Apley, D. W., Chen, W., Lamb, D., and Gorsich, D. (2012). “Improving identifiability in model calibration using multiple responses.” *Journal of Mechanical Design*, 134, 10, 100909.

Bayarri, M., Berger, J., Garcia-Donato, G., Liu, F., Paulo, R., Sacks, J., Palomo, J., Walsh, D., Cafeo, J., and Parthasarathy, R. (2007). “Computer Model Validation with Functional Output.” *Annals of Statistics*, 35, 5, 1874–1900.

Bayarri, M. J., Berger, J. O., Calder, E. S., Dalbey, K., Lunagomez, S., Patra, A. K., Pitman, E. B., Spiller, E. T., and Wolpert, R. L. (2009). “Using statistical and computer models to quantify volcanic hazards.” *Technometrics*, 51, 4, 402–413.

Brynjarsdóttir, J. and O’Hagan, A. (2014). “Learning about physical parameters: The importance of model discrepancy.” *Inverse Problems*, 30, 11, 114007.

Childs, D. (1993). *Turbomachinery Rotordynamics: Phenomena, Modeling, and Analysis*. New York, NY: John Wiley & Sons, Inc.

Conti, S. and O’Hagan, A. (2010). “Bayesian emulation of complex multi-output and dynamic computer models.” *Journal of statistical planning and inference*, 140, 3, 640–651.

Delgado, A., Librashi, M., and Vannini, G. (2012). “Dynamic Characterization of Tilting Pad Journal Bearings From Component and System Level Testing.” *ASME Turbo Expo 2012: Turbine Technical Conference and Exposition*. DOI: 10.1115/GT2012-69851.

D’Souza, R. J. and Childs, D. W. (2002). “A Comparison of Rotordynamic-Coefficient Predictions for Annular Honeycomb Gas Seals Using Three Different Friction-Factor Models.” *Journal of Tribology*, 124, 3, 524–529.

Fadikar, A., Higdon, D., Chen, J., Lewis, B., Venkatramanan, S., and Marathe, M. (2018). “Calibrating a Stochastic Agent Based Model Using Quantile-based Emulation.” *SIAM/ASA Journal on Uncertainty Quantification*, 6, 4, 1685–1706.

Gramacy, R. B. (2020). *Surrogates: Gaussian Process Modeling, Design and Optimization for the Applied Sciences*. Boca Raton, Florida: Chapman Hall/CRC. <http://bobby.gramacy.com/surrogates/>.

Gramacy, R. B. and Apley, D. W. (2015). “Local Gaussian process approximation for

large computer experiments.” *Journal of Computational and Graphical Statistics*, 24, 2, 561–578.

Gramacy, R. B., Bingham, D., Holloway, J. P., Grosskopf, M. J., Kuranz, C. C., Rutter, E., Trantham, M., and Drake, R. P. (2015). “Calibrating a large computer experiment simulating radiative shock hydrodynamics.” *Annals of Applied Statistics*, 9, 3, 1141–1168.

Gu, M. (2019). “Jointly robust prior for Gaussian stochastic process in emulation, calibration and variable selection.” *Bayesian Analysis*, 14, 3, 857–885.

Gu, M. and Berger, J. O. (2016). “Parallel partial Gaussian process emulation for computer models with massive output.” *Annals of Applied Statistics*, 10, 3, 1317–1347.

Gu, M. and Wang, L. (2018). “Scaled Gaussian Stochastic Process for Computer Model Calibration and Prediction.” *SIAM/ASA Journal on Uncertainty Quantification*, 6, 4, 1555–1583.

Guinness, J. (2019). “Spectral density estimation for random fields via periodic embeddings.” *Biometrika*, 106, 2, 267–286.

Higdon, D., Gattiker, J., Williams, B., and Rightley, M. (2008). “Computer model calibration using high-dimensional output.” *Journal of the American Statistical Association*, 103, 482, 570–583.

Higdon, D., Kennedy, M., Cavendish, J. C., Cafeo, J. A., and Ryne, R. D. (2004). “Combining field data and computer simulations for calibration and prediction.” *SIAM Journal on Scientific Computing*, 26, 2, 448–466.

Hirs, G. G. (1973). “A Bulk-Flow Theory for Turbulence in Lubricant Films.” *Journal of Lubrication Technology*, 95, 2, 137–145.

Huang, J., Gramacy, R. B., Binois, M., and Libraschi, M. (2020). “On-site surrogates for large-scale calibration.” *Applied Stochastic Models in Business and Industry*, 36, 2, 283–304. Preprint on arXiv:1810.01903.

Jiang, Z., Arendt, P., Apley, D., and Chen, W. (2016). “Multi-response Approach to Improving Identifiability in Model Calibration.” In *Handbook of Uncertainty Quantification*. New York: Springer.

Johnson, L. (2008). “Microcolony and Biofilm Formation as a Survival Strategy for Bacteria.” *Journal of Theoretical Biology*, 251, 24–34.

Kennedy, M. C. and O’Hagan, A. (2001). “Bayesian calibration of computer models (with discussion).” *Journal of the Royal Statistical Society, Series B*, 63, 3, 425–464.

Kita, H., Taniguchi, K., and Nakajima, Y. (2016). *Realistic Simulation of Financial Markets: Analyzing Market Behaviors by the Third Mode of Science*, vol. 4. Springer.

Kleynhans, G. and Childs, D. (1997). “The Acoustic Influence of Cell Depth on the Rotordynamic Characteristics of Smooth-Rotor/Honeycomb-Stator Annular Gas Seals.” *ASME Journal of Engineering for Gas Turbines and Power*, 949–957.

Liu, F., Bayarri, M., and Berger, J. (2009). “Modularization in Bayesian analysis, with emphasis on analysis of computer models.” *Bayesian Analysis*, 4, 1, 119–150.

Marcy, P. W. and Storlie, C. B. (2020). “Bayesian Calibration of Computer Models with Informative Failures.” Preprint on arXiv:2006.07546.

McFarland, J., Mahadevan, S., Romero, V., and Swiler, L. (2008). “Calibration and uncertainty analysis for computer simulations with multivariate output.” *AIAA journal*, 46, 5, 1253–1265.

Mehta, P., Walker, A., Lawrence, E., Linares, R., Higdon, D., and Koller, J. (2014). “Modeling satellite drag coefficients with response surfaces.” *Advances in Space Research*, 54, 8, 1590–1607.

Morris, M. D. and Mitchell, T. J. (1995). “Exploratory designs for computational experiments.” *Journal of Statistical Planning and Inference*, 43, 381–402.

Paulo, R., Garcia-Donato, G., and Palomo, J. (2012). “Calibration of computer models with multivariate output.” *Computational Statistics and Data Analysis*, 56, 12, 3959–3974.

Petersen, K. B. and Pedersen, M. S. (2008). “The matrix cookbook.” *Technical University of Denmark*, 7, 15.

Plumlee, M. (2017). “Bayesian calibration of inexact computer models.” *Journal of the American Statistical Association*, 112, 519, 1274–1285.

— (2019). “Computer model calibration with confidence and consistency.” *Journal of the Royal Statistical Society: Series B*, 81, 3, 519–545.

Santner, T. J., Williams, B. J., and Notz, W. I. (2018). *The design and analysis of computer experiments, 2nd Edition*. Springer Science & Business Media.

Tuo, R. and Wu, C. F. J. (2015). “Efficient calibration for imperfect computer models.” *Annals of Statistics*, 43, 6, 2331–2352.

— (2016). “A Theoretical Framework for Calibration in Computer Models: Parameterization, Estimation and Convergence Properties.” *Journal of Uncertainty Quantification*, 4, 767–795.

Wong, R. K. W., Storlie, C. B., and Lee, T. C. M. (2017). “A Frequentist Approach to Computer Model Calibration.” *Journal of the Royal Statistical Society: Series B (Statistical Methodology)*, 79, 2, 635–648.

Zhang, Y., Zhao, H., Hassinger, I., Brinson, L. C., Schadler, L. S., and Chen, W. (2015). “Microstructure reconstruction and structural equation modeling for computational design of nanodielectrics.” *Integrating Materials and Manufacturing Innovation*, 4, 1, 14.

## A Appendix: separate calibration results

### A.1 Univariate calibration results: full Bayes for 16 outputs

In this section, we present all univariate  $\mathbf{u}$  posterior distributions separately sampled from 16 outputs, including  $K_d$ ,  $k_c$ ,  $C_d$ , and  $c_c$ , and each at multiple frequencies 28, 70, 126, and 154 Hz. Figure 10 summarizes these results marginally. Observe greater difference between output properties (block), than differences across different frequencies (color) within.

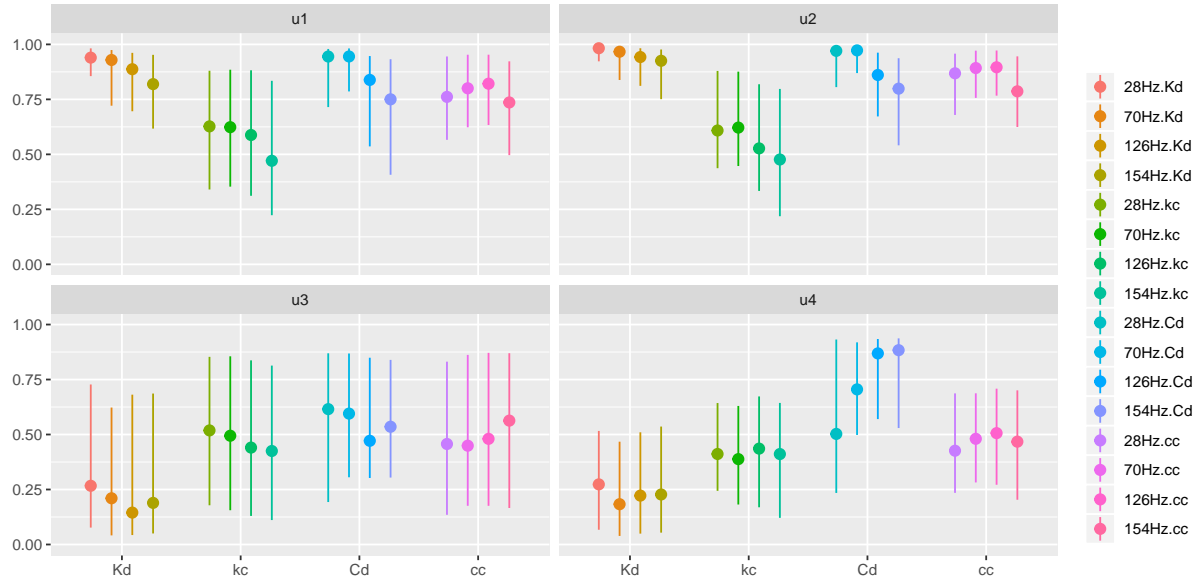


Figure 10: 16 sets of marginal  $\mathbf{u}$  posteriors from outputs  $K_d$ ,  $k_c$ ,  $C_d$ , and  $c_c$  at frequencies 28, 70, 126, and 154 Hz. Dots indicate MAP values and error bars form 90% intervals.

Augmenting those 1d marginals, 11 and 12 projects  $\mathbf{u}$  onto its 6 2d marginals for each frequency. Each row represents a complete set of 2d projections for one output property at one frequency level. Cross frequency consistency in MAP estimation and high density region can be observed from these figures, echoing Figure 10.

## A.2 PC-level calibration results: optimization and full Bayes

We display all 4 sets of PC-calibrated parameters  $\mathbf{u}_j^1$ , for  $j = 1, \dots, J$  using both modular optimization and fully Bayesian approaches developed from Section 4.2 in Figures 13 and 14. To save space, we pair results from stiffness outputs,  $K_d$  and  $k_c$ , into Figure 13 and damping outputs,  $C_d$  and  $c_c$ , into Figure 14. All 4 outputs demonstrate distinct parameter distributions with varying levels of uncertainty. Stronger similarity can be observed between the damping outputs in Figure 14 than the stiffness ones in Figure 13. Compared with the fully integrated results in Figure 8, output cross stiffness  $k_c$  appears to be the most similar to the overall distribution.

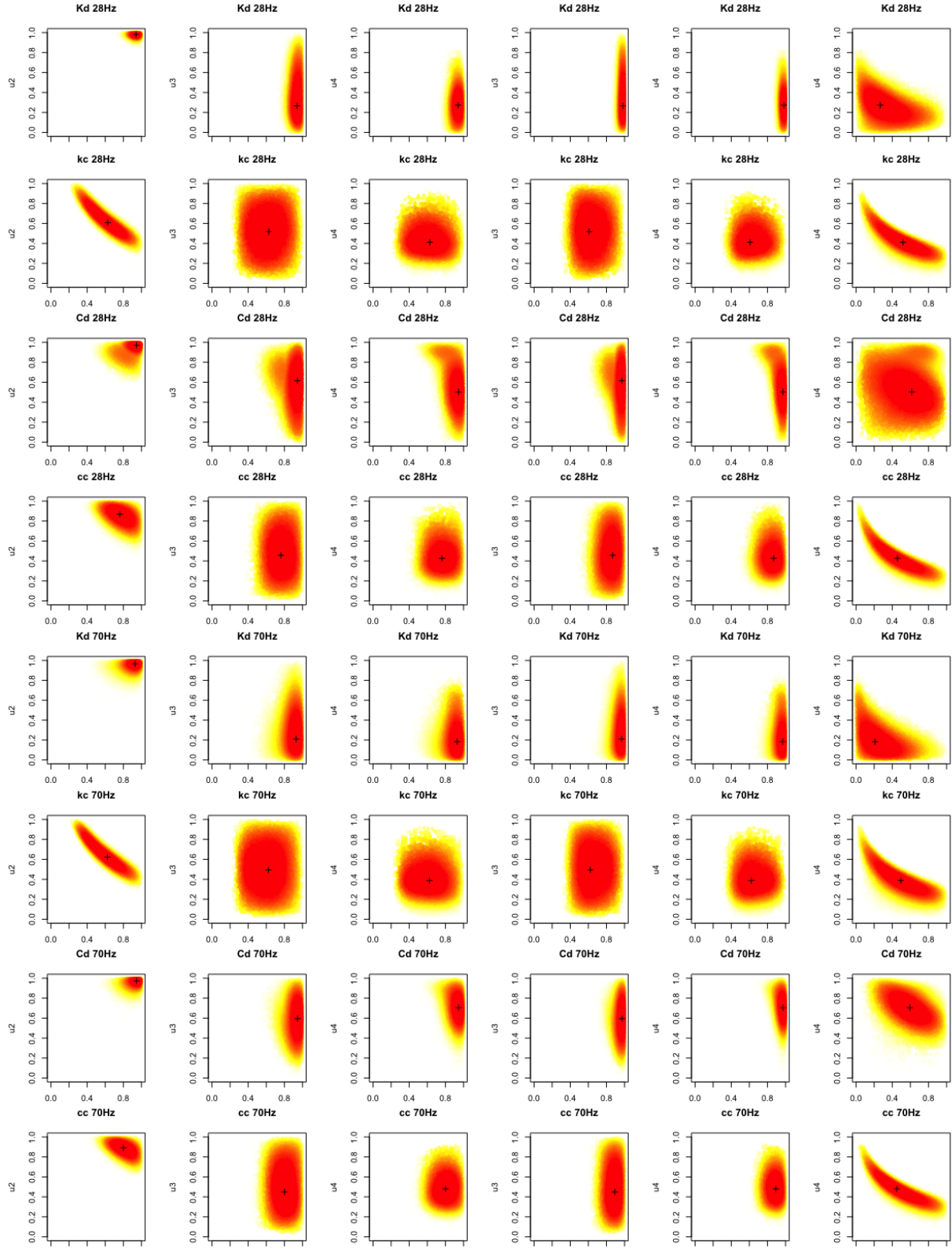


Figure 11: Bivariate marginals of single-output posterior samples of  $\mathbf{u}$  at 28 and 70 Hz.

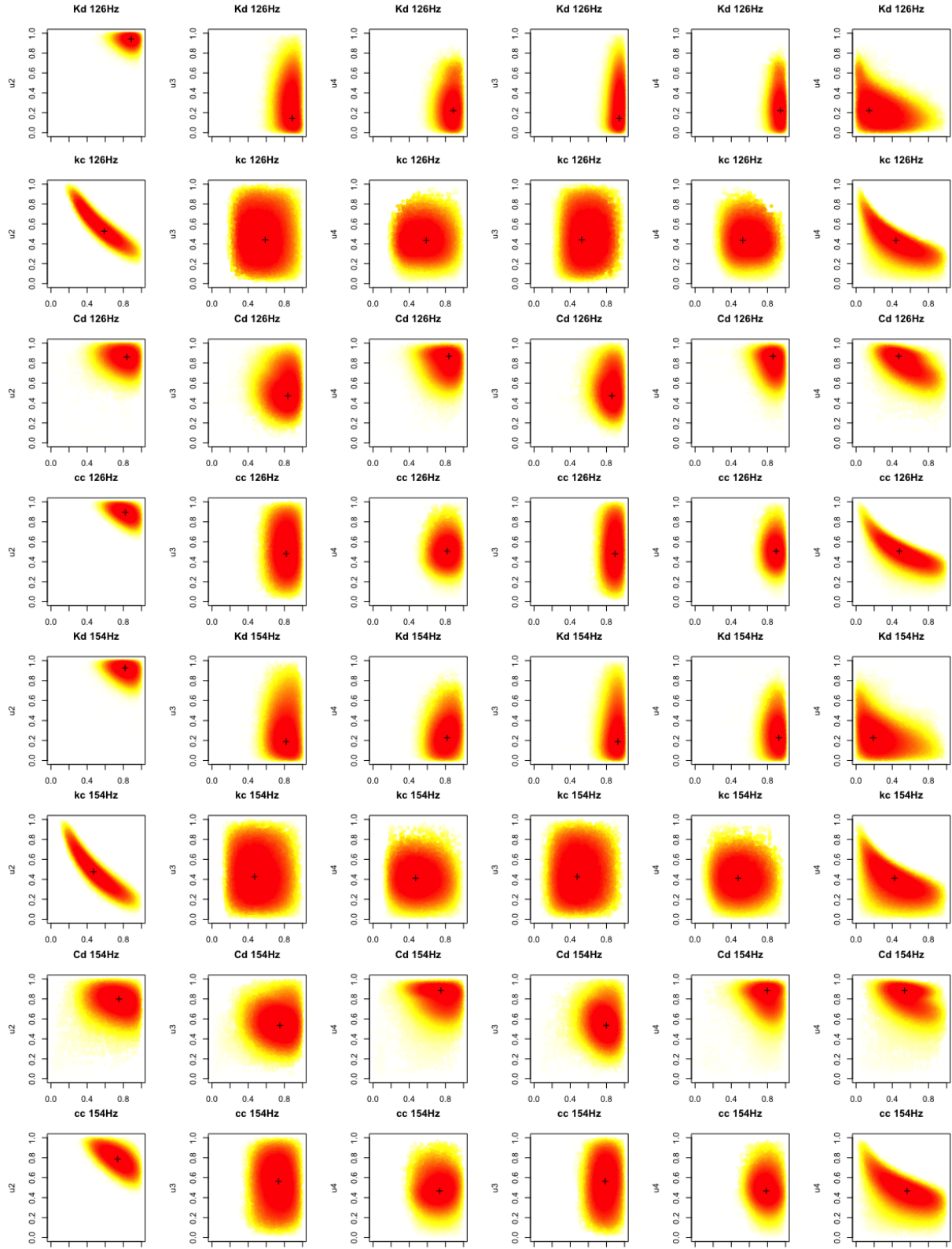


Figure 12: Bivariate marginals of single-output posterior samples of  $\mathbf{u}$  at 126 and 154 Hz.

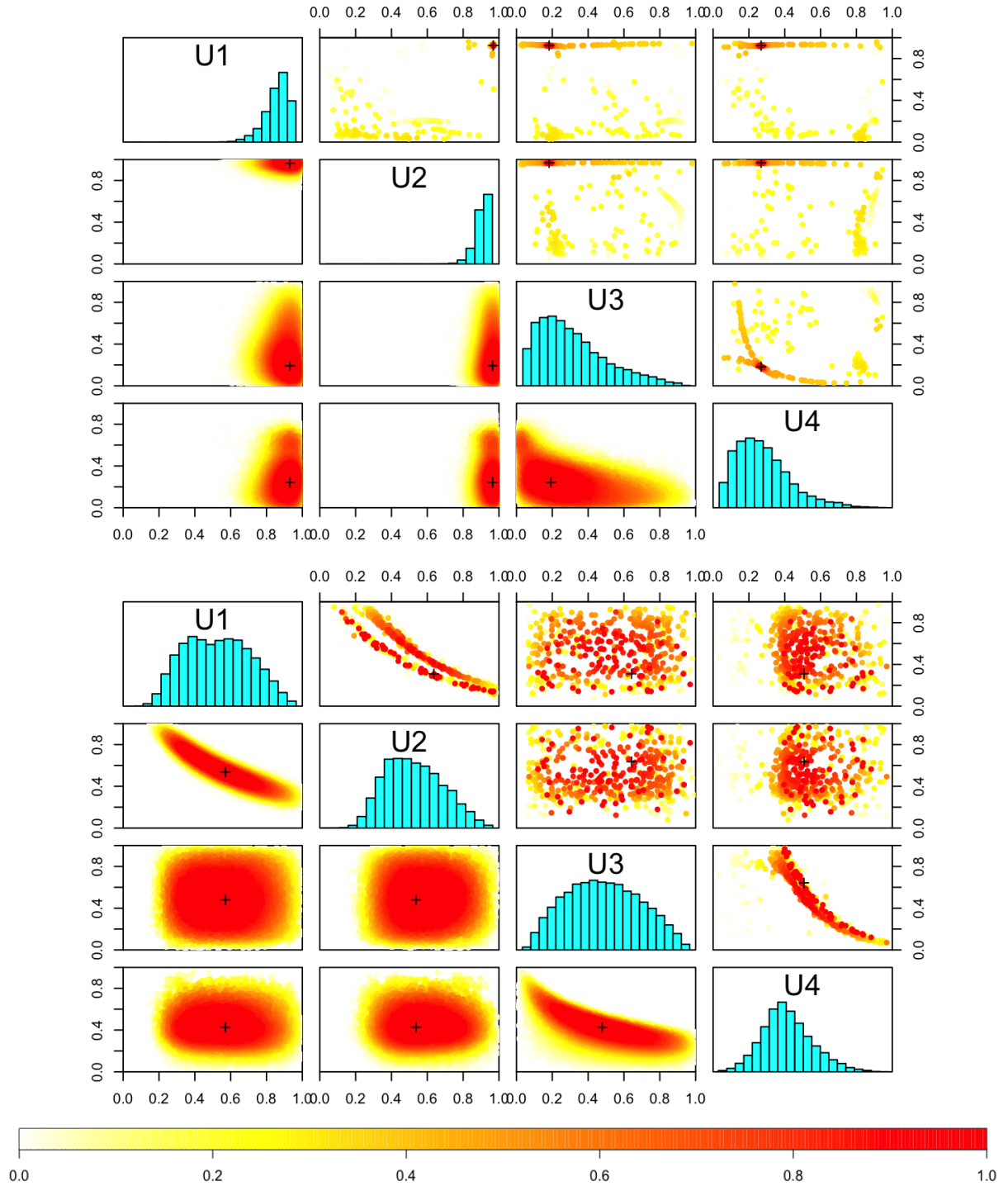


Figure 13: PC fully Bayesian (lower and diagonal) and modular optimization (upper) calibration results representing  $\mathbf{u}_1^1$  for  $K_d$  (top) and  $\mathbf{u}_2^1$  for  $k_c$  (bottom) combining 4 frequencies. Heat color are derived from rank of (joint) log posterior probability of these parameter values. Bayesian results are from 100,000 MCMC samples after burn-in. Optimization results are from 500 converged random multi-starts. “+” signs indicate the MAP values.

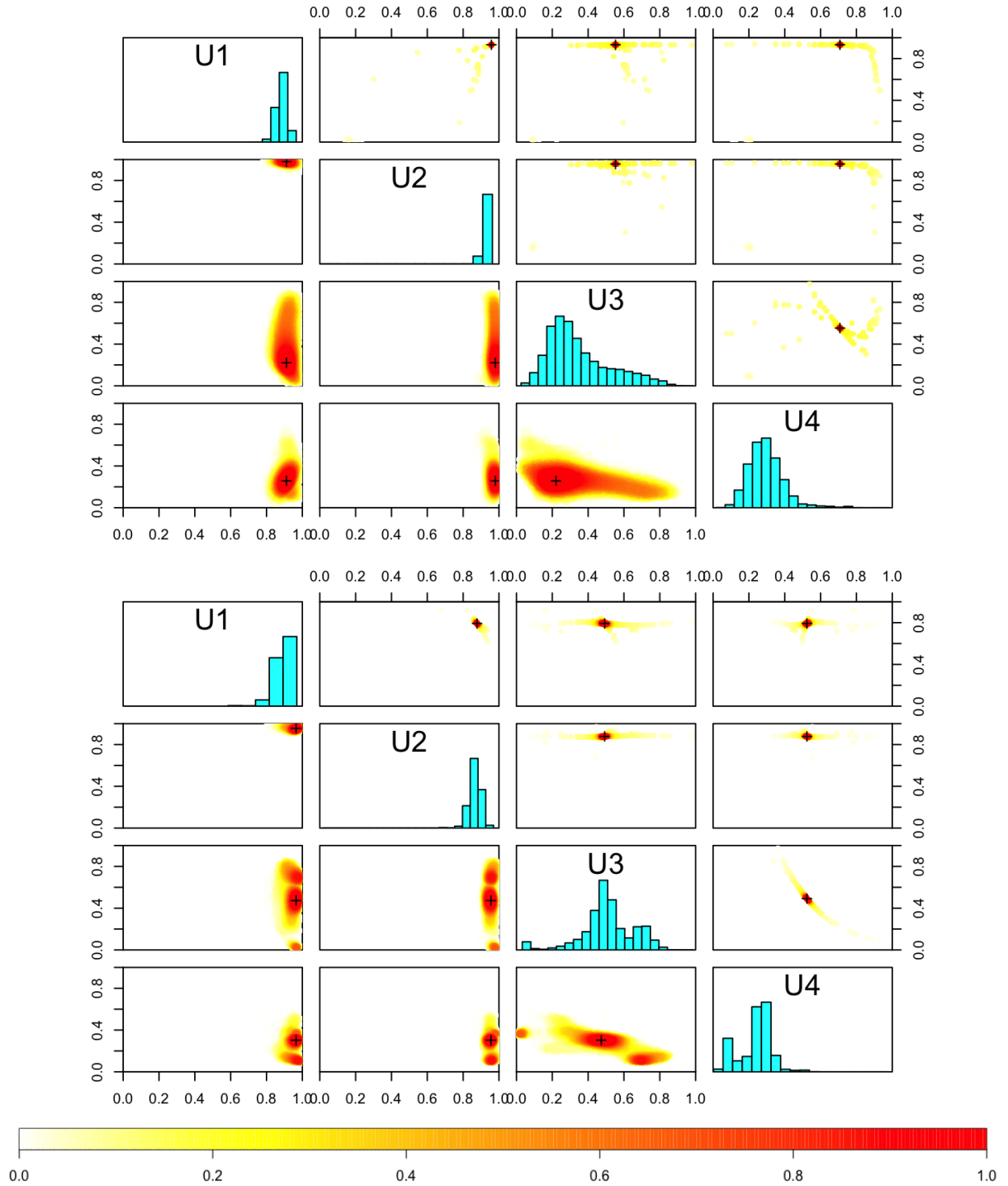


Figure 14: PC fully Bayesian (lower and diagonal) and modular optimization (upper) calibration results representing  $u_3^1$  for  $C_d$  (top) and  $u_4^1$  for  $c_c$  (bottom) combining 4 frequencies. Heat color are derived from rank of (joint) log posterior probability of these parameter values. Bayesian results are from 100,000 MCMC samples after burn-in. Optimization results are from 500 converged random multi-starts. “+” signs indicate the MAP values.